







Article

γ -Valerolactone Production from Levulinic Acid Hydrogenation Using Ni Supported Nanoparticles: Influence of Tungsten Loading and pH of Synthesis

Gerardo E. Córdova-Pérez ¹, Jorge Cortez-Elizalde ¹, Adib Abiu Silahua-Pavón ¹, Adrián Cervantes-Uribe ¹, Juan Carlos Arévalo-Pérez ¹ , Adrián Cordero-García ¹ , Alejandra E. Espinosa de los Monteros ¹, Claudia G. Espinosa-González ² , Srinivas Godavarthi ², Filiberto Ortiz-Chi ² , Zenaida Guerra-Que ³  and José Gilberto Torres-Torres ^{1,*} 

- ¹ Laboratorio de Nanomateriales Catalíticos Aplicados al Desarrollo de Fuentes de Energía y Remedación Ambiental, Centro de Investigación de Ciencia y Tecnología Aplicada de Tabasco (CICTAT), DACB, Universidad Juárez Autónoma de Tabasco, Km.1 Carretera Cunduacán-Jalpa de Méndez, Cunduacan CP 86690, Tabasco, Mexico; enrique_cordova90@hotmail.com (G.E.C.-P.); link-190@hotmail.com (J.C.-E.); adibab45@gmail.com (A.A.S.-P.); adrian.cervantes@ujat.mx (A.C.-U.); carlos.arevalo@ujat.mx (J.C.A.-P.); adrian.cordero@ujat.mx (A.C.-G.); alejandra.espinosa@ujat.mx (A.E.E.d.I.M.)
- ² Investigadoras e Investigadores por Mexico, Universidad Juárez Autónoma de Tabasco, División Académica de Ciencias Básicas, Centro de Investigación de Ciencia y Tecnología Aplicada de Tabasco (CICTAT), Km.1 Carretera Cunduacán-Jalpa de Méndez, Cunduacan CP 86690, Tabasco, Mexico; claudia.espinosa@gmail.com (C.G.E.-G.); godavarthi.srinivas@gmail.com (S.G.); filiberto.ortiz@ujat.mx (F.O.-C.)
- ³ Tecnológico Nacional de México Campus Villahermosa, Laboratorio de Investigación 1 Área de Nanotecnología, Km. 3.5 Carretera Villahermosa-Frontera, Cd. Industrial, Villahermosa CP 86010, Tabasco, Mexico; zenaida.gq@villahermosa.tecnm.mx
- * Correspondence: gilberto.torres@ujat.mx; Tel.: +52-191-4336-0300; Fax: +52-191-4336-0928



Citation: Córdova-Pérez, G.E.; Cortez-Elizalde, J.; Silahua-Pavón, A.A.; Cervantes-Uribe, A.; Arévalo-Pérez, J.C.; Cordero-García, A.; de los Monteros, A.E.E.; Espinosa-González, C.G.; Godavarthi, S.; Ortiz-Chi, F.; et al. γ -Valerolactone Production from Levulinic Acid Hydrogenation Using Ni Supported Nanoparticles: Influence of Tungsten Loading and pH of Synthesis. *Nanomaterials* **2022**, *12*, 2017. <https://doi.org/10.3390/nano12122017>

Academic Editors: Qijie Liang and Chengkuo Lee

Received: 12 May 2022

Accepted: 7 June 2022

Published: 11 June 2022

Publisher's Note: MDPI stays neutral with regard to jurisdictional claims in published maps and institutional affiliations.



Copyright: © 2022 by the authors. Licensee MDPI, Basel, Switzerland. This article is an open access article distributed under the terms and conditions of the Creative Commons Attribution (CC BY) license (<https://creativecommons.org/licenses/by/4.0/>).

Abstract: γ -Valerolactone (GVL) has been considered an alternative as biofuel in the production of carbon-based chemicals; however, the use of noble metals and corrosive solvents has been a problem. In this work, Ni supported nanocatalysts were prepared to produce γ -Valerolactone from levulinic acid using methanol as solvent at a temperature of 170 °C utilizing 4 MPa of H₂. Supports were modified at pH 3 using acetic acid (CH₃COOH) and pH 9 using ammonium hydroxide (NH₄OH) with different tungsten (W) loadings (1%, 3%, and 5%) by the Sol-gel method. Ni was deposited by the suspension impregnation method. The catalysts were characterized by various techniques including XRD, N₂ physisorption, UV-Vis, SEM, TEM, XPS, H₂-TPR, and Pyridine FTIR. Based on the study of acidity and activity relation, Ni dispersion due to the Lewis acid sites contributed by W at pH 9, producing nanoparticles smaller than 10 nm of Ni, and could be responsible for the high esterification activity of levulinic acid (LA) to Methyl levulinate being more selective to catalytic hydrogenation. Products and by-products were analyzed by ¹H NMR. Optimum catalytic activity was obtained with 5% W at pH 9, with 80% yield after 24 h of reaction. The higher catalytic activity was attributed to the particle size and the amount of Lewis acid sites generated by modifying the pH of synthesis and the amount of W in the support due to the spillover effect.

Keywords: hydrogenation; levulinic acid; γ -valerolactone; tungsten; Ni/Al₂O₃-TiO₂ nanocatalysts

1. Introduction

At the beginning of the 21st century, one of humanity's challenges is facing is the production of energy as a consequence of the growing world demand due to the increase in the population. The depletion of oil, one of the main sources of energy, and the impact of CO₂, which is one of the greenhouse gases causing climate change, are some of the factors that make the development of renewable and environment friendly sources of energy one of

the most important challenges of the modern world. All these have led to the expansion of new sources of sustainable energy that protect the environment, such as the use of biomass for this purpose [1]. Lignocellulosic biomass is a promising raw material for the production of high added-value chemicals and biofuels because it is abundant and renewable, and as it is normally a non-used waste it does not belong to any food chain [2]. Levulinic Acid (LA) is a rising platform molecule according to the US Department of Energy [3,4]. Due to its two functional groups (ketone and carboxylic acid) it can be transformed into various high added-value chemicals such as γ -Valerolactone (GVL), 1,4-pentanediol, succinic acid, 3-hydroxypropanoic acid, and 2-methyltetrahydrofuran [5]. LA can be produced by hexoses, which are the key components of cellulose. Catalytic dehydration of hexoses or cellulose results in the formation of 5 HMF [4,6], and through hydration it can form LA [7]. On an industrial scale, several companies around the world have developed processes for the production of levulinic and furfural acid, focusing on viable commercial applications of levulinic acid, such as lactones, levulinate esters, or valeric biofuels [8,9]. Most of these processes involve GVL as an intermediary. LA hydrogenation results in GVL as a product, which is a stable and low-toxic molecule of great application due to its unique physicochemical characteristics, high boiling points (207–208 °C) and flash point (96 °C), low vapor pressure, and air inertia [10,11]. GVL applications are based on the production of liquid biofuels, solvents, food additives, aromatics, or oxygenated gasoline additives [12–15]. GVL is considered a better alternative to ethanol as a fuel additive, because it has a significantly lower vapor pressure and a higher energy density compared with ethanol [16]. Bruno et al. tested the properties of the blend fuel GVL/gasoline and found that the addition of GVL led to a considerable decrease in CO emissions [17].

GVL can be obtained by hydrogenation of LA or by alkyl levulinate using heterogeneous catalysts based on noble metals such as Ru, Au, Ir, Rh, Re, Pd, and Pt [18–22]. Upare et al. reported a 98.6% yield of GVL on Ru/C catalyst using dioxane as a solvent at high H₂ pressures, while when using Pd/C and Pt/C catalysts the yields of GVL were 90% and 30% respectively, so Ru showed a better activity [23]. Yan et al. studied the liquid phase hydrogenation of LA to GVL using methanol as a solvent with a Ru/C catalyst of (5%) with selectivity of 99% to GVL and a LA conversion of 92% in a batch reactor (130 °C, 1.4 Mpa H₂) in methanol. However, the activity and stability of the Ru/C catalyst was not reproducible due to active metal leaching [24]. Lange et al. also reported a serious problem of leaching/deactivation of active metals of the heterogeneous catalyst in LA hydrogenation. Although carbon supports overcome the leaching problem to some extent, they do not allow regeneration of the deactivated catalyst [25].

Despite Ru's excellent catalytic activity under mild reaction conditions, the main challenges are high costs and leaching that can limit its application on an industrial scale.

To avoid using noble metal catalysts, Ni-based catalysts have a relatively higher stability during the reaction as advantages and they can be easily recycled due to their magnetism, making them an alternative for this type of reaction. Mallesham et al. [26] documented that when using the (30%)Ni/SiO₂ catalyst a selectivity of GVL >97% was achieved with a LA conversion of 54.5% during 20 h of reaction.

Fu et al. [27] observed that by using a catalyst (40%)Ni/Al₂O₃ prepared by wet impregnation, a selectivity of 99% of GVL was achieved with a LA conversion of 100% in dioxane during 4 h of reaction (180 °C and 30 bar H₂). Although dioxane improves the stability of nickel catalysts, the use of this solvent is not recommended as it is carcinogenic [28]. Jiang et al. [29] studied Ni/MgO-Al₂O₃ in different ratios of Mg/Al and Ni/MgAlO_{2.5}, obtaining an optimal GVL yield of 99.7% (160 °C, 30 bar H₂). The larger surface area enhanced nickel dispersion on the MgO-Al₂O₃ support, explaining the high activity and selectivity towards GVL compared with Ni/MgO and Ni/Al₂O₃. On the other hand, Lv et al. [30] obtained optimal results (100% conversion of LA and 93.3% selectivity of GVL) using Ni/MgO from a series of prepared catalysts (Ni/SiO₂, Ni/Al₂O₃, Ni/TiO₂, Ni/ZrO₂, and Ni/ZnO) using 2-propanol as solvent and a donor of H₂ at 150 °C for 2 h.

It has been reported that metal leaching can be suppressed during the reaction by using alcohols as solvent [31,32].

Al-Shaal et al. [33] studied the influence of solvents (methanol, ethanol, 1-butanol, 1,4-dioxane, and mixtures of methanol-H₂O, ethanol-H₂O, and butanol-H₂O). Among the alcoholic solvents used, methanol showed the highest LA conversion and GVL yields. This observation was attributed to the high solubility of H₂ in the solvent compared with others used in this study. On the other hand, the use of primary alcohols promotes the esterification of LA. Enumula et al. [34] studied the influence of WO₃ in the catalyst (3%)WO₃/SBA-16 boosting the esterification of LA with ethanol, methanol, propanol, and butanol. Within these solvents, methanol and ethanol achieved the highest selectivity of 96% and 95% respectively.

Meanwhile, Kumar et al. [35] studied the catalyst (20%)Ni/TiO₂ with a conversion of LA of 68.8% and a selectivity to GVL of 88.8%, with (1.5%)WO₃(20%)Ni/TiO₂; the Brønsted sites generated by WO₃ were responsible for opening the GVL ring producing valeric acid (VA) decreasing the selectivity of GVL. Mafokoane et al. [36] obtained similar results using CuO/Al₂O₃-WO₃ (6%) as the catalyst, obtaining a higher conversion of LA, but the selectivity of GVL decreased due to the increase in Lewis-type acidity, creating 2-Methyltetrahydrofuran (2-MTHF). Yuan et al. [37] reported a 100% ring opening and decalin conversion using Ni-WO₃/Al₂O₃-Zeolite at 345 °C, attributed to abundant strong Brønsted acid sites with an increase in WO₃ loading until reaching the 18% by weight. In addition to the importance of the particle size for the hydrogenation of LA to GVL, the acid-base properties and the structural characteristics of the support represent an important role at the moment of hydrogenation [38].

It has been found that the moderate Lewis—Brønsted acidity in the support is responsible for the dehydration of the 4-hydroxy pentanoic acid important intermediate in the production of GVL [39]. A study using Montmorillonite (MMT) showed how strong acidity facilitates LA esterification and cyclization, while Ni metal sites promoted selective hydrogenation of LA to GVL [31]. Enumula et al. [40] found that in the ZrO₂/SBA-15 catalyst the acidity increased with an increase in the percentage of ZrO₂ (25% by weight), improving the selectivity to GVL. However, a further increase in acidity up to 30 wt% ZrO₂ led to the generation of undesired products due to GVL ring opening, which produced a decrease in GVL selectivity.

LA conversion using Ni/Al₂O₃, Cu/Al₂O₃, and Ni-Cu/Al₂O₃ at 250 °C and 6.5 MPa H₂ demonstrated a rapid deactivation of the Ni/Al₂O₃ catalyst caused by a greater formation of carbon on the surface. The NiAl₂O₄ catalyst has been reported to provide greater resistance to carbon formation. Relatively large particle sizes > 10 nm facilitate carbon formation [41,42], not only it providing better efficiency in hydrogenation by spillover effect, but also resistance to carbon deposition.

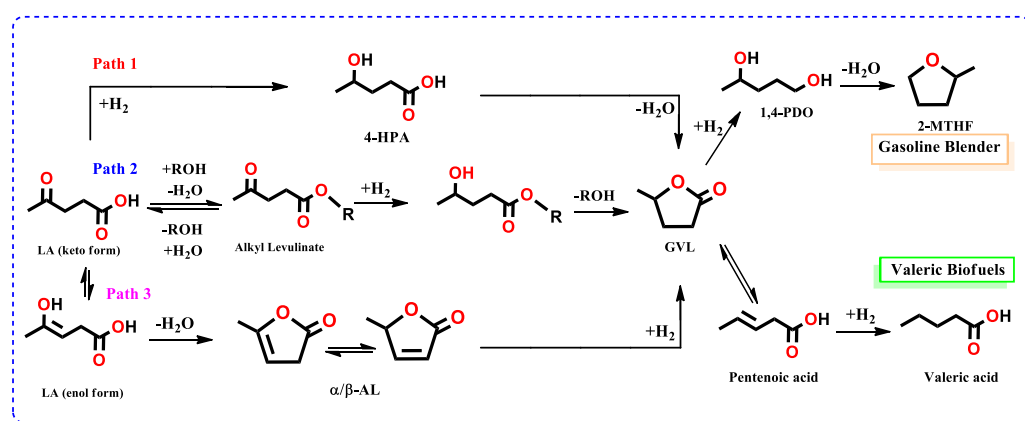
Hengst et al. [43] studied various synthesis methods and the (5%)Ni/Al₂O₃ was the best catalyst prepared by the wet impregnation modified with urea, showing a 90% LA conversion and 75% GVL yield (140 °C and 30 bar H₂) using dioxane as solvent for 4 h. The use of urea showed a larger surface area besides obtaining a particle size of 7 nm, which were important factors in the catalytic activity. In fact, several studies emphasized the importance of smaller particle sizes <10 nm, which promote better performance in the hydrogenation of LA or its alkyl levulinates to GVL [44–46].

Table 1 shows different Ni-based monometallic supported catalysts and experimental conditions selected for the synthesis of the GVL using LA as the platform molecule. These previous studies evaluated different loadings of Ni and types of supports showing catalytic performance effects.

Table 1. Ni-based monometallic supported catalyst and experimental conditions selected for the synthesis of the GVL using LA as platform molecule.

Catalyst	Substrate	Solvent	H ₂ Source	T [°C]	Time [h]	GVL Yield (%)	LA Conversion (%)	Ref.
Ni/Al ₂ O ₃ (40 wt.% Ni)	LA	H ₂ O	50 bar H ₂	200	4	57%	57%	[47]
Ni/HAP (5 wt.% Ni)	LA	Methanol	10 bar H ₂	150	6	5%	100%	[48]
Ni/TiO ₂ (5 wt.% Ni)	LA	Methanol	10 bar H ₂	275	3	13%	21%	[49]
Ni/TiO ₂ (10 wt.% Ni)	LA	H ₂ O	-	270	15	23%	26%	[49]
Ni/TiO ₂ (10 wt.% Ni)	LA	H ₂ O	-	270	15	48%	54%	[49]
Ni/Al ₂ O ₃ (30 wt.% Ni)	LA	Methanol	40 bar H ₂	120	4	80%	89%	[50]
Ni/Al ₂ O ₃ (10 wt.% Ni)	LA	-	8 bar H ₂	140	5	11%	18%	[51]
Ni/SiO ₂ (10 wt.% Ni)	LA	-	8 bar H ₂	140	5	8%	8%	[51]
Ni/CeO ₂ (10 wt.% Ni)	LA	-	8 bar H ₂	140	5	5%	18%	[51]
Ni/SiO ₂	LA	-	100 bar H ₂	250	5	100%	89	[52]

The catalyst support is key in Scheme 1, which shows the different reaction routes. Route 1 is the hydrogen reduction of the carbonyl group to obtain an intermediate 4-hydroxylevulinic acid (4-HPA) followed by intramolecular esterification to obtain GVL. Route 2 is carried out by the esterification of LA by the alcohol functional group followed by hydrogenation and subsequently dealcoholization, promoting GVL formation. Route 3 involves dehydration of LA to Angelica Lactone (α/β -AL) and after that hydrogenation of the double bond C=C to give GVL [46]. Oxides such as Al₂O₃, ZrO₂, TiO₂, and their mixtures TiO₂-ZrO₂, Al₂O₃-TiO₂-W, and WO₃-Ta₂O₅ have been tested in biomass decomposition, obtaining good results [6,53–56].

**Scheme 1.** Pathway's reaction of the GVL.

Hun et al. [57] showed that Al₂O₃ works as a good acid support due to the formation of Brønsted (-OH) and Lewis (Penta coordinated Al³⁺) acid sites that can promote dehydration which can occur during GVL synthesis, according to path 1 and 3.

Improved catalytic activity in LA conversion and selectivity to GVL has been related to well-dispersed metal particles and their size along with the combination of Lewis acid-base sites. Nowadays, due to the high price of noble metals and metal leaching, the production of GVL has been replaced with the use of transition metals such as Fe, Cu, Co, and Ni [58].

Consequently, the novelty of the present work falls in several points: (1) we used Ni as a transition metal, (2) we used methanol as a reaction medium due to its high selectivity to Alkyl Levulinate (AL), which is an important intermediate in the production of GVL [34], as can be seen in path 2, (3) we synthesized Ni using a suspension impregnation method that has not been reported before and has led to generation of particle sizes lower than 10 nm, and (4) we used a complex three-component support (Al₂O₃-TiO₂-WO₃), varying the W content and the PH of the medium synthesis of supports, creating variability of acidity levels of the support and reducibility of metal that is beneficial for GVL yield.

In fact, it has been proved that support is able to modify the properties of the active phase such as its reducibility, dispersion, and stability due to a closed intimate interaction

between the metal particles and the support. The support plays an important role to obtain a better dispersion of the metallic phase associated with the lattice defects or structural defects in nanomaterials, such as oxygen vacancies or unsaturated sites. Additionally, the modification of one oxide support using the doping of support enhances more the activity, selectivity, and stability of the catalysts [53,54]. The strong metal support interaction is beneficial to avoid metal leaching [59,60].

Therefore, this work studied the addition of W in the Ni/Al₂O₃-TiO₂-WO₃ catalyst to different pH values of support synthesis and its effect on the amount of Lewis acid sites and the Ni particle size in the GVL yield. Methanol was used as the reaction medium because there is little information on the conversion of LA to GVL. Considering all the above, we presented a series of Ni/Al₂O₃-TiO₂-WO₃ catalysts with a load of 10% Ni and 1%, 3%, and 5% W as a bifunctional active catalyst in the conversion of LA to GVL and its esterification of methyl levulinate at 170 °C and 4 MPa of H₂ in a batch reactor during 24 h of reaction. The by-products were analyzed by H¹ nuclear magnetic resonance. The catalysts were prepared using the suspension impregnation method and characterized by nitrogen physisorption, adsorbed pyridine by Fourier transform infrared spectroscopy (FT-IR), X-ray diffraction (XRD), UV-vis spectroscopy with diffuse reflectance (DRS UV-Vis), temperature-programmed reduction of hydrogen (TPR-H₂), temperature-programmed desorption of hydrogen (TPD-H₂), Scanning Electron Microscopy (SEM), Transmission Electron Microscopy (TEM), and X-ray Photoelectron Spectroscopy (XPS).

2. Materials and Methods

2.1. Reagents

All reagents used were of analytical quality and were used without any purification treatment: Levulinic acid (Sigma-Aldrich, Toluca city, Mexico, 99.5% purity), Gamma-valerolactone (Sigma-Aldrich, 99.5% purity), Angelica-lactone (Sigma-Aldrich, 99.5% purity), Methanol (Meyer, 99.9% purity), Aluminum trisecbutoxide C₁₂H₂₇AlO₃ (Sigma-Aldrich, 97% purity), Titanium butoxide (IV) Ti[O(CH₂)₃CH₃]₄ (Sigma-Aldrich, 97% purity), hydrated ammonium metatungstate (NH₄)₆(NH₄)₆H₂W₁₂O₄₀·xH₂O, nitrate nickel (II) hexahydrate Ni(NO₃)₂·6H₂O, n-butanol (99.9%, Baker), and Sec-butanol (Sigma-Aldrich, 99.5% purity). All experiments were performed using ultrapure water (18.2 MΩ cm⁻¹) from a PureLab model Option-Q water purifier.

2.2. Catalyst Support Synthesis

Sol-Gel method was used for the synthesis of the Al₂O₃-TiO₂-WO₃ support, modifying the pH to 3 and 9 using acetic acid [CH₃COOH] and ammonium hydroxide [NH₄OH] respectively. The Al₂O₃/TiO₂ ratio was 50/50 by weight, while the percentage of W was 1%, 3% and 5% by weight. The synthesis was carried out in aqueous medium, using 1-butanol [CH₃-(CH₂)₃-OH] and 2-butanol [CH₃CH₂CH(OH)CH₃] as solvent with ultra-pure water to conduct the hydrolysis between the butoxide titanium [Ti(OCH₂CH₂CH₂CH₃)₄] and the aluminum tri-sec-butoxide Al[OCH(CH₃)C₂H₅]₃ (Sigma-Aldrich, 97% purity). The water/alcohol molar ratio was 1/8 by volume and alkoxide/water was 1/16. The alcohol/alkoxide mixture was added to a flask with constant stirring until a homogeneous mixture was obtained. Once the mixture was homogenized, the water was added slowly over 3 h. The pH of the water was adjusted to pH 3 and pH 9 respectively and, immediately afterwards, the hydrated ammonium metatungstate salt ((NH₄)₆H₂W₁₂O₄₀ • xH₂O) was added until it was completely dissolved. After the dripping, it was left under constant stirring for 24 h at a temperature of 80 °C. Once the gel was formed, the solvent was removed in a rotary evaporator at 80 °C and left to dry in an oven at 120 °C for 48 h. Finally, it was calcined at 500 °C with a heating ramp of 2 °C/min. Table 1 shows the labels of materials.

2.3. Ni Supported Catalysts Preparation

Ni catalysts supported on Al₂O₃-TiO₂-WO₃ were prepared by the suspended impregnation method [61]. The support was heated in a reducing atmosphere with hydrogen flow at 90 mL/min using a heating ramp of 2 °C/min, until reaching a temperature of 300 °C and it remained in this way for 1 h. Subsequently, the support was cooled to a temperature of 25 °C, changing the nitrogen flow for 30 min. Nickel nitrate salt Ni(NO₃)₂·6H₂O was added in 20 mL of water, and calculations were carried out to have a 10% by weight of nickel in relation to the support. It was kept under nitrogen flow for 10 min, and later mixed with the support under nitrogen flow to have a homogeneous mixture. After 30 min, the nitrogen flow was changed to hydrogen. It was brought to a temperature of 80 °C and kept for 12 h in order to evaporate the water. Then, the reduction of the material was carried out in a reducing atmosphere of hydrogen with a flow of 90 mL/min with a ramp of 2 °C/min until reaching 450 °C for 4 h. Finally, the catalyst was cooled to 25 °C in a hydrogen flow, then removed, stored, and labeled. All the catalysts prepared for this study, as well as their labels, are shown in Table 2.

Table 2. Textural properties: Surface area S_{BET} , Pore volume P_v , Average pore diameter P_d of Al₂O₃-TiO₂-WX basic and acid supports.

Supports	WO ₃ Loading (Wt%)	S_{BET} (m ² g ⁻¹)	P_v (cm ³ g ⁻¹)	P_d (nm)
ATW1 A ^a	1	386.9	0.84	5.9
ATW3 A ^a	3	381.9	0.80	5.9
ATW5 A ^a	5	370.6	0.76	5.6
ATW1 B ^b	1	365.1	0.76	5.8
ATW3 B ^b	3	352.7	0.95	7.9
ATW5 B ^b	5	323.3	0.78	7.0

a: pH 3 (CH₃COOH), b: pH 9 (NH₄OH).

2.4. Characterization Techniques

2.4.1. Nitrogen Physisorption

The determination of the specific area, diameter, and pore volume of the catalysts was conducted by the N₂ physisorption technique. It was performed on equipment of surface area measurement, MICROMERITICS TRISTAR 3020 II at 77 K (−196 °C). To remove impurities, a 0.1 g sample was weighed and degassed for 3 h at 300 °C. Data were analyzed in ASAP 2020 software to determine specific area (Sg), pore volume (Vp), and pore size distribution (PSD) using the B.E.T. method (Brunauer, Emmet, and Teller).

2.4.2. X-ray Diffraction (XRD)

X-ray diffraction analysis was used to determine the composition of the phases and to estimate the crystallite size of the powders. X-ray diffraction (XRD) was performed using a Bruker D2 PHASER diffractometer with Co K α radiation source ($\lambda = 0.179$ nm) during an analysis time of 660 s. The analysis was carried out in the range of 20° to 80°. The JADE 6 database helped to complete the identification of the phase. The average size of the crystals in the catalysts was estimated using the Scherrer equation:

$$D = \frac{0.9}{\cos\theta} \quad (1)$$

2.4.3. Diffuse Reflectance UV-Vis Spectroscopy (DRS UV-Vis)

The UV-Vis Diffuse Reflectance Spectra were performed on a Varian Cary 300 spectrophotometer, in the range of 800 to 200 nm, equipped with an integrating sphere. BaSO₄ compound with 100% reflectivity was used as a reference.

2.4.4. SEM (Scanning Electron Microscopy)

SEM micrographs of the samples were recorded using a Scanning Electron Microscope (JEOL, USA Inc., Peabody, MA, USA, model JSM-6010LA).

2.4.5. X-ray Photoelectron Spectroscopy (XPS)

The XPS spectra of the samples were recorded using a SPECS[®] spectrometer with a PHOIBOS[®] 150 WAL hemispheric energy analyzer with angular resolution (<0.5 degrees), equipped with an XR 50 X-ray Al-Ray and μ -FOCUS 500 X-ray monochromator (Al excitation line). To protect the fresh and spent sample it was transferred to the XPS chamber without exposing it to air (using a mobile XPS chamber under Ar). The binding energy of C 1s (284.8 eV) was used as a reference. Binding energies (B_E) and intensities for chemical quantitation were determined after subtracting a Shirley-type background from the photoemission spectra using XPS peak 4.1 software.

2.4.6. Pyridine FTIR Analysis

Solid samples were analyzed by FTIR using pyridine as a probe molecule to determine the acid properties of samples following the method according to which the samples are analyzed in the form of self-supporting tablets, previously subjected to in situ activation under vacuum at 400 °C before absorbing pyridine. All the analyses were carried out on a NICOLET FTIR equipment model Magna 560 with a resolution of 4 cm⁻¹ and 50 scans, and a DTGS detector.

2.4.7. Temperature Programed Reduction of Hydrogen (TPR-H₂)

The reduction at programmed temperature of hydrogen (TPR-H₂) of the monometallic catalysts was completed in Bel Japan Belcat-B equipment equipped with a thermal conductivity detector (TCD). The experiments were carried out using 50 mg of reduced catalyst. It was heat treated in a cell with argon for one hour at 400 °C, using a heating rate of 10 °C/min and an argon flow of 50 mL/min. It was cooled to room temperature and passed through a flow of the 5% H₂/95% Ar mixture. TPR thermograms were recorded using a heating ramp at 10 °C/min with a temperature range of 50 to 900 °C with a flow rate of 10 mL/min.

2.4.8. Temperature Programed Desorption of Hydrogen (TPD-H₂)

The desorption at programmed temperature of hydrogen (TPD-H₂) of the monometallic catalysts was completed in a Bel Japan Belcat-B equipment equipped with a thermal conductivity detector (TCD). The experiments were carried out using 50 mg of reduced catalyst. It was heat treated in a cell with argon for one hour at 550 °C, using a heating rate of 10 °C/min and an argon flow of 50 mL/min. It was cooled to 40 °C and passed through a flow of the 5% H₂/95% Ar mixture of 20 mL/min for 1 h. Finally, a flow of Ar was passed for 1 h ($T = 40\text{ C}$, $Ar_{\text{flow}} = 50\text{ mL/min}$). TPD thermograms were recorded using a heating ramp at 10 °C/min with a temperature range of 50 to 500 °C with a flow rate of 50 mL/min of Ar for 45 min.

2.4.9. High Resolution Transmission Electron Microscopy (HRTEM)

TEM analysis was performed using JEM-2100 (JEOL, Tokyo, Japan) equipment operating at an acceleration voltage of 200 kV. The powder was treated with a sonication in isopropanol to ensure a homogeneous dispersion. A small drop was deposited on the carbon films on a 200-mesh copper grid, which was introduced into the TEM Analysis chamber after complete evaporation of the solvent.

2.5. Catalytic Tests

All the hydrogenation reactions from LA to GVL were carried out in a stainless-steel autoclave of 50 mL high pressure, equipped with a magnetic stirring system. The reaction was executed using 0.6 g of LA in a solution of 30 mL of methanol, applying 0.2 g of catalyst

with a 3:1 ratio (LA/catalyst). The reaction was completed at a temperature of 175 °C, with a stirring of 500 rpm under a 40 bar pressure of H₂. The reaction was monitored for 24 h, and samples were taken at different times.

2.5.1. Analysis of the LA and GVL after Reaction Tests

Gas Chromatographic Analysis (GC)

The reaction crude was filtered after the reaction, when the reactor was cooled to room temperature, to later be analyzed in a Shimadzu GC-2010 Plus gas chromatograph, equipped with a FID detector and a capillary column HP-5 19091J-413 (30 cm × 0.32 mm × 0.25 μm). The initial temperature of the column was 80 °C with a temperature ramp of 10 °C/min, with an injection volume of 0.5 μL; the SPLIT injector temperature was 250 °C and the detector temperature was 270 °C with a flow of 30 mL/min of H₂ and 300 mL/min of air, and the carrier gas was He with a flow of 25 mL/min.

The conversion of levulinic acid and yield of GVL were calculated using the following equations:

$$\% \text{ GVL yield} = \frac{\text{Moles of GVL produced}}{\text{Inicial moles of LA}} \quad (2)$$

$$\% \text{ LA Conversion} = \frac{\text{Moles of LA reacted}}{\text{Inicial moles of LA}} \quad (3)$$

Hydrogen Nuclear Magnetic Resonance ¹H-NMR Analysis

The solvent was evaporated at the reaction crude and subsequently analyzed by ¹H NMR to identify the products of the conversion from LA to GVL and the by-products generated. A Bruker Advance III 600 MHz NMR spectrometer was employed using deuterated chloroform (CDCl₃, 25 °C). The spectra were processed with the MestReNova program ¹H NMR (600 MHz, CDCl₃).

3. Results and Discussions

3.1. Catalysts Characterization

3.1.1. N₂ Physisorption

The form of the isotherms of the ATW A and ATW B supports were analyzed, showing type IV isotherms typical of mesoporous materials (2–50 nm) according to IUPAC [62]. Isotherms in Figure 1a reveal two types of hysteresis in all the supports in both synthesis methods due to the geometry of the titanium having a hysteresis loop H1 (P/P₀) of 0.7, indicating the large size of the inlet of the pores in a spherical and continuous way because of the interaction of WO₃ and TiO₂ as shown by previous studies [36,63,64]. On the other hand, a hysteresis loop of the H2 type, representative of solids with non-uniform cylindrical pores due to the interaction of Al₂O₃-TiO₂, with a bottleneck shape appeared [65,66]; this hysteresis loop was located between a relative pressure (P/P₀) of 0.8–0.9 in the supports and indicates the pore interconnectivity [67]. The surface area increased with the percentage of WO₃, obtaining a larger surface area in the supports modified at pH 3 in contrast with the supports at pH 9 (See Table 2). These results are consistent with those reported by another research group, who observed that a greater surface area was obtained using acetic acid to set the pH at 3 [68].

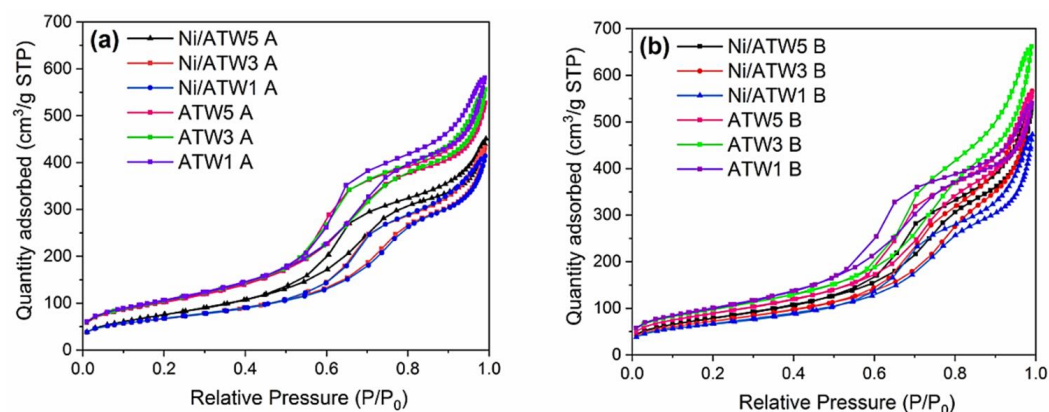


Figure 1. (a) Adsorption–Desorption Isotherms of the acid supports (ATWXA) and monometallic catalysts (Ni/ATWXA) and (b) basic (ATWXB) supports and monometallic (Ni/ATWXB) catalysts.

Figure 1b shows the isotherms of the Ni catalysts and that, like the isotherms of the supports, they did not have changes in the type of isotherm with the nickel deposit. This indicates that there was a good thermal stability and despite the reductive treatment at 450 °C, they still have type IV isotherms, characteristic of mesoporous materials. All the isotherms of the supported Ni catalysts presented a hysteresis loop of type H1 and type H2 in a range of (P/P^0) 0.5–1, which indicates that the porous structure of the materials was maintained. The isotherms showed a decrease due to the obstruction of the pores by the nickel deposit, generating pores of smaller size with respect to the support. According to the results, the stability of the structure is a result of thermal stability, because of the synergy between $\text{TiO}_2\text{-Al}_2\text{O}_3$ and its interaction with Ni particles. The high percentage of titanium could be a factor, among others, that result in thermal stability of supported Ni catalysts, as mentioned by Escobar et al. [68]; on the other hand, Zhang et al. [42] prepared Ni/ Al_2O_3 catalysts, preserving the structure and geometry of the catalyst pores, despite the Ni deposit at temperatures above 700 °C; this thermal stability is consequence of the strong interaction between Ni and Al_2O_3 in concentration of 35% to 50% *w/w* of nickel and at temperatures from 400 °C to 800 °C. The structure is maintained due to the presence of NiAl_2O_4 , bringing stability and integrity to the structure up to high temperatures. The decrease of a certain percentage (~37%) in the surface area of the Ni/ATW1 A and Ni/ATW3 A catalysts regarding the support is due to the blocking of the pores by the metallic charge. Only a loss of (~14%) was observed for the Ni/ATW5 material in which there was the highest amount of tungsten. As seen in Table 3, greater stability is obtained when the support contains tungsten (5% *w/w*). The pore volume decreases, and the pore diameter increases at concentrations < 5%, which could indicate a partial collapse of the pores due to the smaller pore diameter as the effect of pH which, in this case, is 3. Similarly, Li et al. [69] observed that by incorporating Ce on the surface of Al_2O_3 , the decrease in surface area is related to the good dispersion of the metallic charge on the surface, diffusing into the pores.

Table 3. Textural properties: Surface area S_{BET} , Pore volume P_v , and Average pore diameter P_d of Ni/ $\text{Al}_2\text{O}_3\text{-TiO}_2\text{-WX}$ basic and acid monometallic catalysts.

Catalysts	WO_3 Loading (Wt%)	S_{BET} ($\text{m}^2 \text{g}^{-1}$)	P_v ($\text{cm}^3 \text{g}^{-1}$)	P_d (nm)
Ni/ATW1 A ^a	1	245.95	0.59	6.89
Ni/ATW3 A ^a	3	245.98	0.59	6.88
Ni/ATW5 A ^a	5	321.59	0.64	5.74
Ni/ATW1 B ^b	1	244.31	0.62	7.60
Ni/ATW3 B ^b	3	282.36	0.77	8.39
Ni/ATW5 B ^b	5	317.18	0.73	7.20

a: pH 3(CH_3COOH), b: pH 9(NH_4OH).

3.1.2. X-ray Diffraction (XRD)

Figure 2a,b show the X-ray diffraction results of the Monometallic materials prepared with 10% Ni by the suspension method. Signals are observed at $2\theta = 44.5^\circ$, 51.8° , and 76.3° corresponding to the planes (111), (200), and (220) respectively. These peaks were identified using the technical sheet JCPD-04-0850, which belongs to the Ni metallic species with an FCC crystalline phase (face-centered cubic), and this metallic Nickel structure is present in all materials as well as in supports prepared at pH 3 (see Figure 2b) and at pH 9 (see Figure 2a). Weak signals were found assigned to the γ - Al_2O_3 JCPD 10-0339 phase, the presence of which even after the incorporation of Ni may be due to a phase transition between the γ - Al_2O_3 phase and NiAl_2O_4 because it is well dispersed on the support. The existence of the NiAl_2O_4 spinel crystalline phase would originate diffraction peaks coinciding with those attributed to Al_2O_3 with gamma phase. This is because the pseudo-spinel structure of γ - Al_2O_3 has lattice parameters very similar to those of NiAl_2O_4 spinel, which makes both species indistinguishable. However, a slight displacement of the diffraction peaks at smaller angles and an increase in the intensity of the diffraction peak at 46.8° in contrast with the peak at 66.7° may indicate an enrichment in NiAl_2O_4 species versus γ - Al_2O_3 [70] and TiO_2 due to the reducing treatment that was given to the support, causing the dehydroxylation of the surface. The oxygen vacancies generated would induce Ni dispersion and formation of the NiAl_2O_4 spinel [71].

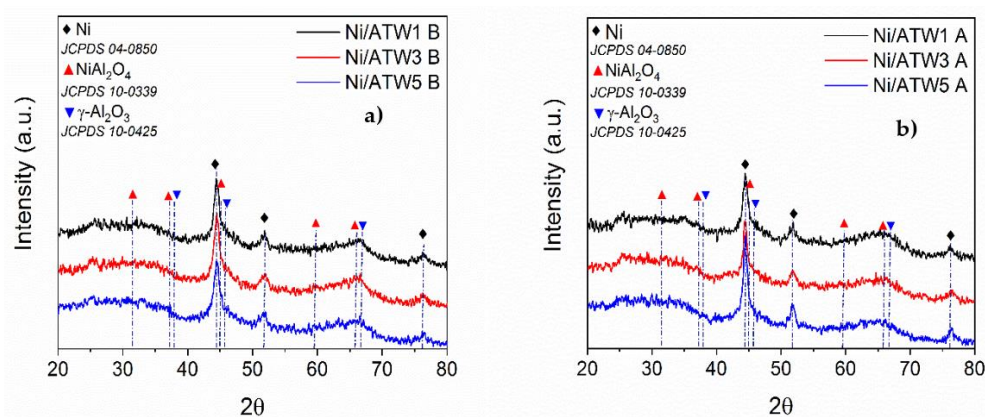


Figure 2. XRD patterns of the monometallic basic and acid catalysts (a) Ni/ATW B and (b) Ni/ATW A.

According to these considerations, it can be stated that since NiO phase is not detected, and it could be possibly found in nanoparticles, undetectable by this technique, dispersed on a support, part of them reduced to metallic Ni and diffused on the Al_2O_3 matrix, forming NiAl_2O_4 .

3.1.3. Diffuse Reflectance UV-Vis Spectroscopy (DRS UV-Vis)

Figure 3a,b show the results of the UV-Vis DRS spectra of the Ni/ATW catalysts. In the range of 375–450 nm and 700–750 nm, Ni species are related in octahedral coordination ($\text{Ni}^{2+}_{\text{oct}}$) and in the range of 450–700 nm they are associated to a tetrahedral coordination ($\text{Ni}^{2+}_{\text{tetra}}$) due to its electron configuration of $3d^8$ [72–75]. Gullapelli et al. [74] used a Ni/ Al_2O_4 and Ni/ TiO_2 catalyst where the position of the bands at 350–450 nm and 700 nm favored the coordination of Ni^{2+} species; the coordination relationship is based on temperature and on nickel charge. Obtaining NiO at a metal load greater than 20% in w/w and less than this load favors the formation of NiAl_2O_4 according to Gullapelli et al. [74]. The modification of the band at 220–350 nm and 360–380 nm in Ni catalysts is related to NiO in octahedral coordination, and the increase in intensity at 345 nm could be related to the growth of NiO, while on the other hand at 510 nm it is related to v_2 (${}^3\text{A}_{2g} \rightarrow {}^3\text{T}_{1g}$) transitions with an octahedral coordination [76]; this species could not be identified in X-ray diffraction, so this band is associated to the nickel spinel (NiAl_2O_4).

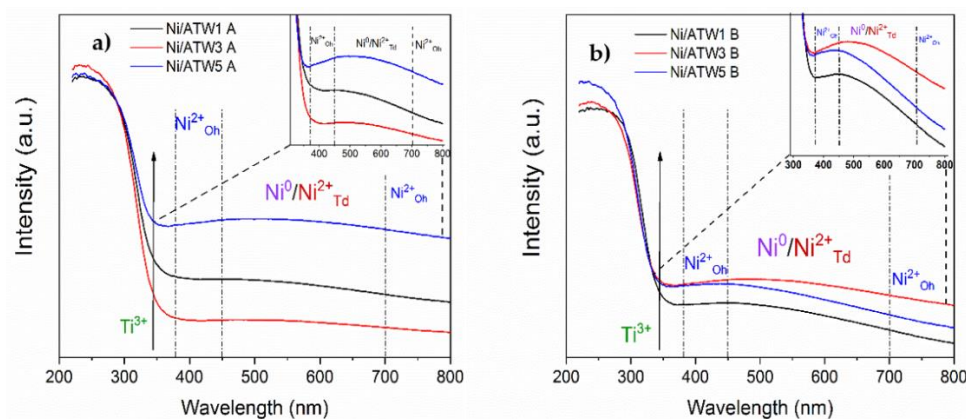


Figure 3. UV-Vis DRS spectrums of the monometallic acid and basic catalysts (a) Ni/ATW A and (b) Ni/ATW B.

As stated by Zurita-Mendez et al. [77] and Scheffer et al. [78], the modification in the 220–350 nm region with respect to the support is due to the charge transfer d–d (${}^3A_{2g}/{}^1T_{1g}$) of $O^{2-} \rightarrow Ni^{2+}$ of Ni^{2+}_{oct} sites that are associated with $NiAl_2O_4$. The intense region at 450–700 nm was associated with the bands of ν_3 (${}^3A_{2g} \rightarrow {}^3T_{1g}(P)$) and ν_2 (${}^3A_{2g} \rightarrow {}^3T_{1g}$) that resulted from the d–d transitions of Ni^{2+} ions contained in octahedral sites, which could conclude the existence of Ni^{3+} species that the octahedral sites are occupied by Ni^{3+} within nickel aluminate $NiAl_2O_4$. These bands are caused by the absorption of Ni^{2+} in coordination Ni^{2+}_{tetra} and Ni^{3+}/Al^{3+} in octahedral coordination [72], as confirmed by the results of Ray diffraction and Raman spectroscopy (not shown here). Then again, the effect of W, on the support, is clear due to the band at 370–450 nm that could be the contribution of the interaction of Ni^{2+} coordinated Ni^{2+}_{oct} with tungsten species, which can form $NiWO_4$. This species has bands characteristics at 280 nm, 370 nm, and 740 nm according to studies by Scheffer et al. [78]; however, the X-ray diffraction results did not identify patterns assigned to this phase.

The intensity of the bands at 500 nm could be related to the oxygen vacancies generated by the reduction of Ti^{4+} to Ti^{3+} as a result of the reduction of Ni^{2+} to Ni^0 [79]. The increase in the absorption band may be due to the degree of vacancies generated by the Ti^{3+} species, distorting the network and causing defects resulting from the change in oxidation state from Ti^{4+} to Ti^{3+} [80].

3.1.4. TPR- H_2

Figure 4a shows the reduction profiles of hydrogen consumption of the Ni/ATW1 A catalyst, and it is observed that the reduction of NiO to Ni^0 was in the range of 300–450 °C; this reduction was carried out in a single step ($NiO + H_2 \rightarrow Ni + H_2O$), being in a lower proportion and with a smaller particle size since, according to the results found in the literature, it is mentioned that a large particle size requires a higher reduction temperature. Corresponding to the XRD technique, no signals were observed to the NiO crystal structure, which is why they are found in sizes smaller than 3 nm in relation to the detection limit of the technique.

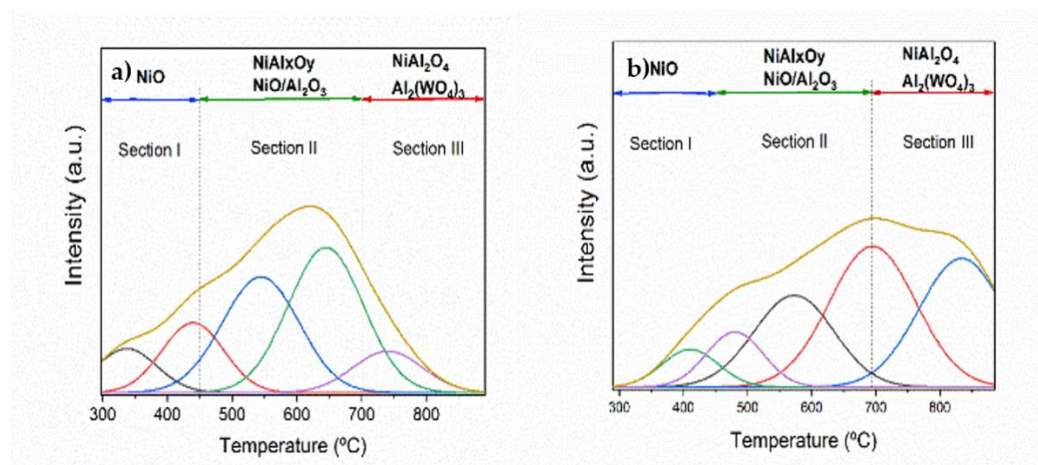


Figure 4. TPR-H₂ profiles of the monometallic acid catalysts (a) Ni/ATW1 A and (b) Ni/ATW5 A.

As claimed by Ewbank et al. [81], “free” NiO is that nickel that is found on the surface of the catalyst in the form of nickel oxide at a reduction temperature lower than 450 °C; therefore, in section I located in a temperature range between 300 and 450 °C, the reduction of NiO to Ni is located on the surface of the support, which has a lower interaction. Additionally, the literature mentions the reducibility of Ni species supported on γ -Al₂O₃ and how it varies depending on the metallic charge. Zeilnski et al. [82] mentioned how a uniform layer of stoichiometric nickel aluminate is created only on the surface of γ -Al₂O₃ when there is a Ni load of 20% by weight. Gao et al. [83] mentioned that the reduction of these species is found in section II located at a temperature between 450 and 750 °C due to a soft interaction with the support, mainly with NiO-Al and NiO-W but with a high content of NiO; this area is associated with the reduction of Ni²⁺ species that are found forming a non-stoichiometric surface aluminate (NiAl_xO_y), highly dispersed on the surface of the support [82]. Kumar et al. [84] and Yang et al. [85] reported that these species are reduced at temperatures above 550 °C, so that W, when in contact with Ni, promotes its dispersion and interaction with the support. In the same way, reduction of Ti⁴⁺ to Ti³⁺ takes place in this area at a temperature of 550 °C generated due to spillover effect, the activation of H₂ on Ni sites, which homolytically dissociates H₂ [86–88]. For the peak located in section III, they have a strong interaction, so a reduction temperature higher than 700 °C is needed [88], and the least reducible NiO is in the NiAl₂O₄ stoichiometry phase, requiring high temperatures for its reduction; the contribution recorded at 750 °C is associated with the reduction of the Ni of spinel NiAl₂O₄ in bulk or stoichiometric form; there was no defined peak at lower temperatures because the Ni particles were dispersed by the Ti and W species, which can obstruct the formation of spinel, promoting the dispersion of nickel [35,89].

The profiles obtained from the Ni/ATW5 A catalyst are shown in Figure 4b, and it can be observed that the increase in the percentage of W 1% to 5% of the support makes more evident the displacement of the reduction peaks at higher temperatures compared with the profiles of the monometallic Ni/ATW1 A catalyst. The deconvolution of the reduction profiles of Ni/ATW5 A revealed a proportion of free NiO in the section I, and the reduction peaks in this section decreased as the percentage of W in the support increased; it is possible that Ni is dispersed in areas of TiO₂ or W [35]. In section II, an increase in the reduction peaks was observed due to a greater interaction of the NiO particles with the support, and the increase in W generated a better dispersion of Ni on the support which promoted the reduction of Ti⁴⁺ to Ti³⁺ due to electron transfer from Ni atoms [89], and charge transfer from Ti⁴⁺ to WO₃ [64] is also possible. In section III, it is shown how the reduction peaks increased compared with when the support had 1% W, so it is possible that the presence of W during the synthesis of Ni/ATW5 A promoted the rearrangement of the γ -Al₂O₃ phase and the interaction of Ni, resulting in the formation of NiAl₂O₄ which, unlike NiAl_xO_y, requires temperatures above 700 °C for its reduction. These results

indicate that a temperature of 450 °C is insufficient for complete Ni reduction with 5% tungsten, and that temperatures higher than 700 °C are needed for when the percentage of $\text{WO}_3 > 1\%$; this may be due to the fact that the increase in WO_3 promotes the stability of the NiAl_2O_4 phase [90]. Because of the octahedral and tetrahedral coordination of Ni^{2+} , higher temperatures are required for its reduction; according to Horsley et al. [91], only 30% of nickel species are reduced at temperatures of 400 °C with 11% nickel, which suggests that 70% of nickel is in the oxidized state, and the profile shift at higher temperatures with 5% W proposes a reduction of large groups of NiO particles and also that the particles interact with tungsten up to certain point in the reduction of NiO. The shift of the reduction peak towards high temperatures with increasing W loading is probably due to an interaction between tungsten oxide and nickel particles [35].

3.1.5. Temperature-Programmed Desorption of Hydrogen (TPD- H_2)

Figure 5 shows the TPD- H_2 profile of Ni/ATW1 A and Ni/ATW5 B catalysts, where a peak located at 120 °C was identified in both catalysts. This peak at low temperature is due to the desorption of H_2 formed from the H atoms adsorbed on the Ni nanoparticles [92] formed from the reduction of free NiO and non-stoichiometric NiAl_2O_4 . It can also be associated with the adsorption/desorption of H_2 , which are related to the morphology and different sizes of metallic particles [93]. No other peaks were observed in the profiles at temperatures above 300 °C, the highest desorption occurred at a temperature of 120 °C.

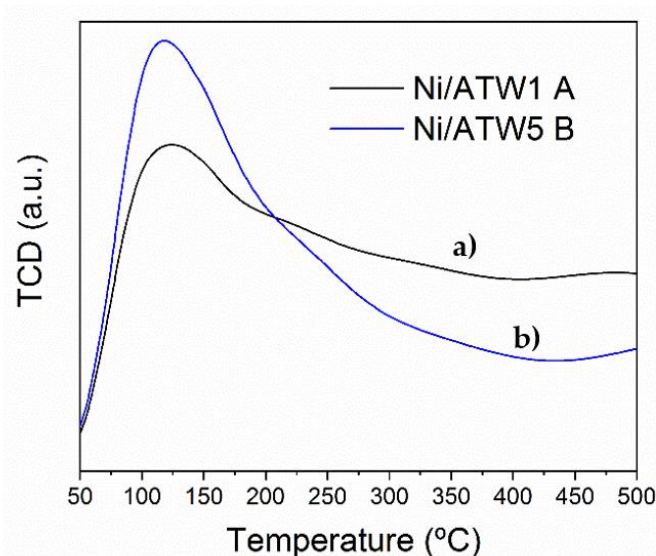


Figure 5. TPD- H_2 profiles of the monometallic acid catalysts (a) Ni/ATW1 A and (b) Ni/ATW5 A.

The low dispersion of Ni is due to the few metallic species available on the surface. Salvati et al. [20] mentioned that for an 11% Ni/ Al_2O_3 catalyst, only 30% of the Ni^{2+} is reduced to the metallic state, and this agrees with the TPR profiles of H_2 where a strong interaction of Ni with the support was observed.

The increase in W content in the Ni/ATW5 B nanomaterial caused an increase in the intensity of the peak at 120 °C with respect to the Ni/ATW1 A nanomaterial, this result suggesting that it has more available metal sites [92]. Crisóstomos et al. [94] attributed the peaks in a range of temperatures (<400 °C) to the desorption of nickel particles dispersed on the support that come from the reduction of non-stoichiometric NiAl_2O_4 that corresponds to a stronger metal–support interaction having resistance to sintering [42].

The metallic dispersion and particle size of Ni/ATW A and Ni/ATW B are reported in Table 4. The dispersion of metallic surface species from Ni/ATW1 A and Ni/ATW5 B was 11.5% and 12.5% respectively, although the Specific Surface Area of 245 m^2/g and 317 m^2/g was high. This effect may be due to the tungsten species that are formed using different pH during the synthesis of the supports [95]. These results suggest that the W

in the basic medium due to the effect of the hydroxyl groups on the surface could help the incorporation of Ni into the framework of a support lattice, due to the presence of extra oxygen vacancy sites caused for the addition of another oxide during the support synthesis method, which helps Ni dispersion and consequently decreases the particle size and increases the dispersion, as suggested by Chary et al. [93] using a catalyst with 10% w/w of Ni supported on Al_2O_3 .

Table 4. Particles size (PS, nm) calculate by XRD patterns of Ni, TEM and TPD- H_2 and Dispersion metallic bi TPD- H_2 of the Ni/ATWX A acid and Ni/ATWX B basic catalysts. Lewis site ($\mu\text{mol/g}_{\text{cat}}$) and $\text{Density}_{\text{LAS}}$ (density of lewis acid site, $\mu\text{mol/m}^2$).

Catalyst	$\text{PS}_{\text{Ni}}^{\text{a}}$ (nm)	$\text{PS}_{\text{Ni}}^{\text{b}}$ (nm)	$\text{PS}_{\text{Ni}}^{\text{c}}$ (nm)	$\text{D}_{\text{Ni}}^{\text{d}}$ (%)	Lewis $\mu\text{mol/g}_{\text{cat}}$	$\text{Density}_{\text{LAS}}$ ($\mu\text{mol/m}^2$)
Ni/ATW1 A	9.4	9.3	8.7	11.5	N.D	N.D
Ni/ATW3 A	10.4	N.D	N.D	N.D	207.1	0.84
Ni/ATW5 A	9.8	11.9	N.D	N.D	428.9	1.74
Ni/ATW1 B	8.8	10.2	N.D	N.D	286.8	0.89
Ni/ATW3 B	8.3	N.D	N.D	N.D	458.9	1.87
Ni/ATW5 B	9.9	8.5	8.2	12.5	445.5	1.57

a: Particle size calculated by XRD patterns of Ni (111) plane by Scherrer's equation, b: Particle size calculated by TEM, c: Particle size calculated by TPD- H_2 , d: Dispersion metallic by TPD- H_2 .

3.1.6. Scanning Electron Microscopy (SEM)

The micrographs shown in Figure 6 correspond to monometallic catalysts. Larger particles are observed in Figure 6a corresponding to the Ni/ATW1 A catalyst, in contrast to the Ni/ATW5 B catalyst of Figure 6b. This effect is due to the use of NH_4OH modifying the textural properties, diffusing the nickel in a more effective way within the pores because the volume and average pore diameter are slightly higher, as previously discussed according to the results of physisorption of N_2 , which contributed to a better dispersion of nickel. Higher concentrations of Ni were observed in abundant areas of titanium, which confirms that metallic nickel is mainly found on the surface of titanium and Ni^{2+} is in strong interaction with Al_2O_3 , forming the spinel as observed in the EDS analysis of backscattered electrons (BSE) where the high contrast in the micrographs is due to the heavier elements of Figures 7 and 8.

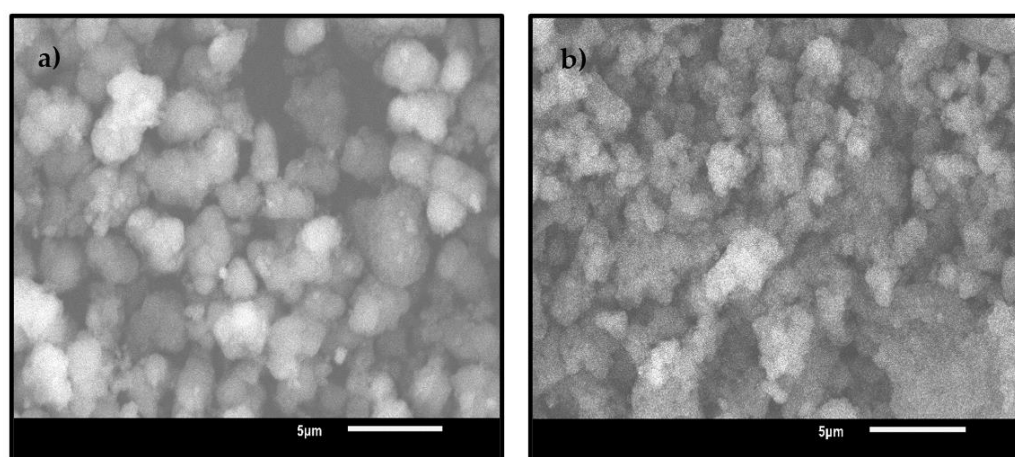


Figure 6. SEM micrography of the monometallic acid and basic catalysts (a) Ni/ATW1 A and (b) Ni/ATW5 B.

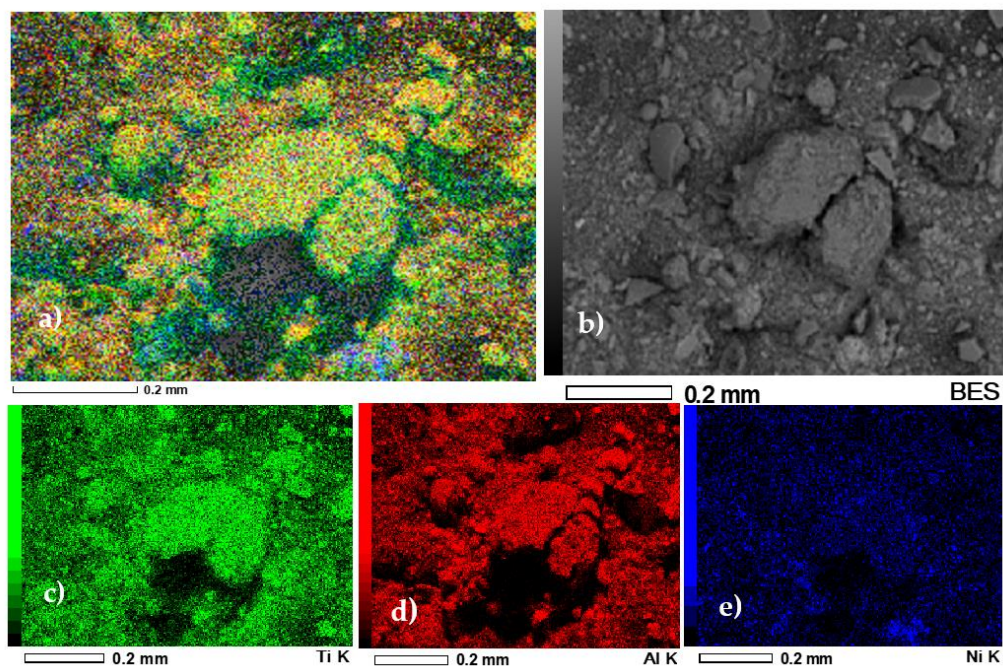


Figure 7. Elemental chemical mapping of the monometallic Ni/ATW1 A acid catalyst. (a) Mixture of all metals (Al, Ti, W and Ni) on the surface analyzed, (b) Surface of Ni/ATW1 A analyzed, (c) Ti distribution on the surface analyzed, (d) Al distribution on the surface analyzed and (e) Ni distribution on the surface analyzed.

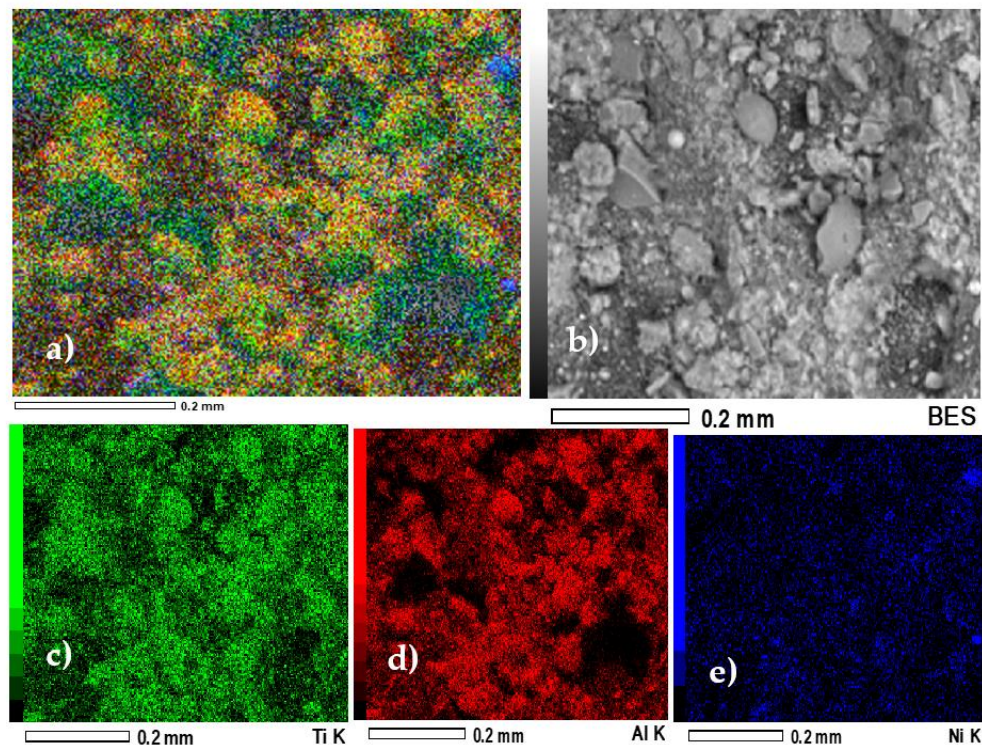


Figure 8. Elemental chemical mapping of the monometallic Ni/ATW5 B basic catalyst. (a) Mixture of all metals (Al, Ti, W and Ni) on the surface analyzed, (b) Surface of Ni/ATW5 B analyzed, (c) Ti distribution on the surface analyzed, (d) Al distribution on the surface analyzed and (e) Ni distribution on the surface analyzed.

In Figure 7a, corresponding to the Ni/ATW1 A catalyst, the results suggest that the elements that compose the support (Al, Ti, and W) were homogeneously distributed. Nickel in Figure 7e is scattered on the surface, both Ti, Al, and W; however, areas of greater accumulation were observed, and the parts of greater contrast are Ni in the metallic state. Zurita et al. [77] suggested that these clear areas are due to NiO particles, but according to the X-ray diffraction results, this phase was not identified, and instead only the Ni and NiAl₂O₄ phases were. According to these results, the lighter parts in the micrographs were caused by the Ni metallic species dispersed on the surface of the support as shown in Figure 7b,e. The darker parts were due to Al₂O₃ and TiO₂, on the other hand, the more agglomerated part implied a strong interaction of Ni and Al, producing the formation of the NiAl₂O₄ spinel, as suggested by Liao et al. [96] when using Ni/Al₂O₃ at 8% by weight Ni; this signified that the Ni²⁺ species have the tendency to join Al₂O₃ using percentages below 15% by weight. Gullapelli et al. [74] mentioned that spinel formation could begin at low temperatures, forming a non-stoichiometric NiAl₂O₄ spinel at the surface level when Ni²⁺ contacts the support at temperatures below 500 °C. Therefore, the spinel would be found in the monolayer of the support, the free NiO is easily reducible, as well as Ni(OH)₂, and these two species are preferentially formed on TiO₂ as indicated by Spanou et al. [97].

In Figure 7c,d Nickel is shown dispersed in the same way as Ti, which suggests the interaction of Ni with Ti, promoting the formation of metallic nickel. The interaction between Ni and Ti and the reduction of Ti⁴⁺ to Ti³⁺ are related due to the reduction of Ni²⁺ to Ni⁰ [79]; the similarity of the micrographs, taking into account the distribution of the elements between Ti and Ni, implies that metallic nickel forms mostly on Ti; on Al it tends to mostly form a NiAl₂O₄ spinel. Escobar et al. [73] mentioned that the modification of the Ni/Al₂O₃ catalyst with TiO₂ with 25% by weight, improves the distribution and reduction of the metal, and this could indicate that Ti can occupy vacancies in the Al₂O₃ network, which avoids the formation of NiAl₂O₄. This same effect was observed up to 0.1% of Ti in Co/Al₂O₃. The results obtained in the Ni/ATW1 A and Ni/ATW5 B micrographs propose that the reduction of Ni was more favorable over TiO₂ and W because they inhibit the formation of the spinel phase.

In Figure 8a the micrographs of the Ni/ATW5 B catalyst are presented, as well as the results of the Ni/ATW1 A catalyst, suggesting a good dispersion of the elements that form the support (Al, Ti, and W). Nickel, on the other hand, Figure 7e, is homogeneously dispersed on the surface, and Ni nanoparticles are visibly in the lighter areas. In Figure 7e due to atomic contrast, nickel is preferentially dispersed over TiO₂ and Al₂O₃. Nickel on the surface of the Ni/ATW5 B catalyst is lower compared with that of Ni/ATW1 A because of the diffusion of nickel within the pores of the support and the greater volume and pore diameter because of NH₄OH and percentage of W. The parts of lower contrast are attributed to the support Al₂O₃-TiO₂-WO₃; in Figure 8b, the areas of high contrast, more agglomerated, suggest a strong interaction of Ni and Al due to the presence of NiAl₂O₄. As proposed by Liao et al. [96], Ni²⁺ species have a tendency to integrate inside of the Al₂O₃ structure.

3.1.7. HRTEM

The results of the HRTEM micrographs of the monometallic catalysts Ni/ATW1 A and Ni/ATW5 A can be seen in Figures 9a–d and 10a–d respectively. Figures 9a and 10a show the monometallic catalyst Ni/ATW1 A and Ni/ATW5 A respectively, at a magnification of 200 nm. Dispersed particles can be observed, as well as agglomerated particles on the surface of the support.

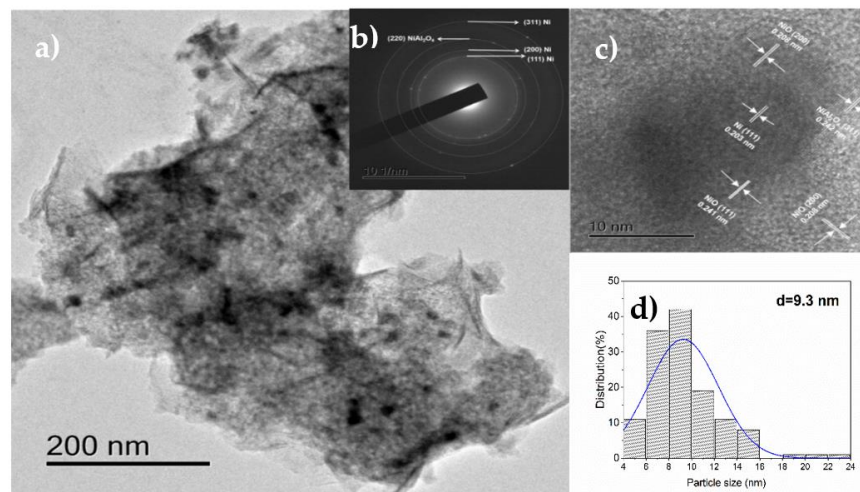


Figure 9. TEM pictures of the monometallic Ni/ATW1 A acid catalyst. (a) Particles of Ni on the surface of catalyst, (b) Electron diffraction patterns of Ni and NiAl₂O₄, (c) Interplanar distance measured of Ni⁰, NiO and NiAl₂O₄ and (d) Histogram distribution of metal particle size and average diameter of Ni.

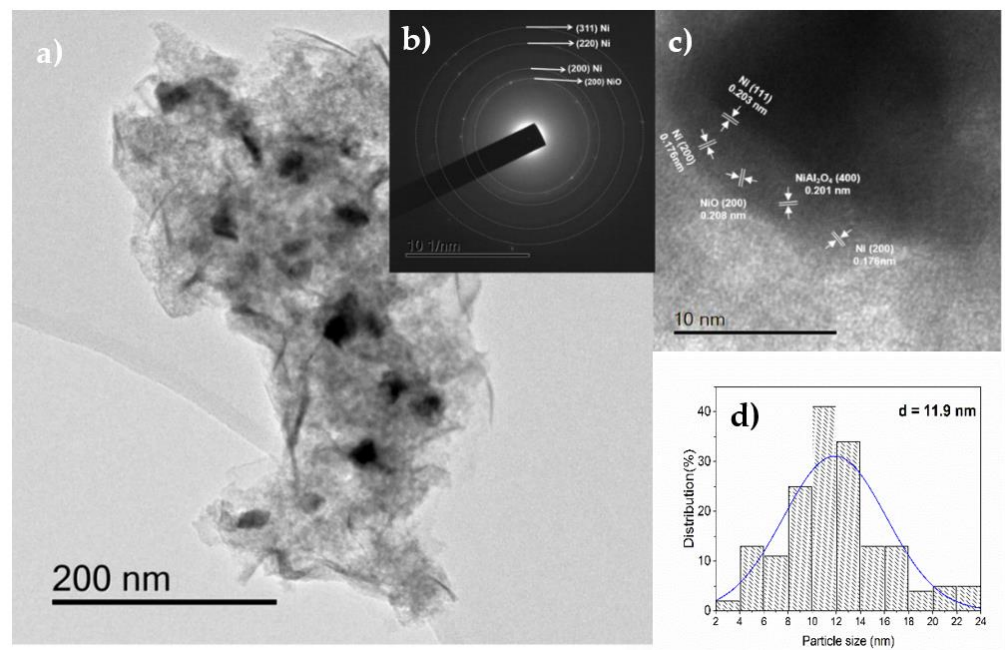


Figure 10. TEM pictures of the monometallic Ni/ATW5 A acid catalyst. (a) Particles of Ni on the surface of catalyst, (b) Electron diffraction patterns of Ni and NiO, (c) Interplanar distance measured of Ni⁰, NiO and NiAl₂O₄ and (d) Histogram distribution of metal particle size and average diameter of Ni.

In Figure 9b four rings were identified that correspond to the Ni phase with planes (111), (200), and (311) and NiAl₂O₄ with planes (220) having a polycrystalline material. The identification of NiAl₂O₄ in Figure 9b coincides with the XRD results, confirming the peak at $2\theta = 65.5^\circ$ that was associated with the phase of the spinel NiAl₂O₄ [70] overlapping with the signal at $2\theta = 67^\circ$ of the phase γ -Al₂O₃ due to non-stoichiometric spinel formation of NiAl₂O₄. In Figure 9c three phases were identified that correspond to NiO with an interplanar distance of 0.208 nm and 0.241 nm with planes indexed in (111) and (200) [98], Ni metallic with plane (111) with an interplanar distance of 0.203 nm and NiAl₂O₄ with plane (311) with an interplanar distance of 0.242 nm. The areas with high

contrast correspond to the characteristic interplanar distance of Ni of 0.203 nm with plane (111), and the reduction of Ni is carried out in the particles with less NiO interaction.

For the Ni/ATW5 A catalyst, in Figure 10a,b, the planes (200) of the NiO structure and planes (200), (220), and (311) of Ni⁰ were identified, being a polycrystalline material as the catalyst Ni/ATW1 A. In Figure 10c three present phases were identified, with interplanar distances of 0.203 nm and 0.176 nm that correspond to the Ni structure of planes (111) and (200), respectively. Additionally, the NiO phase with an interplanar distance of 0.208 nm corresponds to plane (200) and NiAl₂O₄ at 0.201 nm corresponds to plane (400). The 0.176 nm distance was close to the interplanar distance of Ni(OH)₂, so the 0.208 nm planes of NiO, which were located close to it, were due to the reduction of Ni(OH)₂ during synthesis. Zhou et al. [99] stated that Ni formation occurs due to the reduction of NiO formed by the dehydration of Ni(OH)₂ at a temperature of 400 °C, the nucleation of NiO is generated in different directions due to the polycrystalline characteristic of Ni(OH)₂. Most of Ni diffuses into Al₂O₃, and occupying available sites forming NiAl₂O₄, W, and TiO₂ could inhibit the growth of the NiAl₂O₄ spinel; therefore, we can observe that NiO is surrounded by NiAl₂O₄ at the Ni limit, so the Ni metallic nanoparticles originate mainly from NiO dispersed on the surface of the support with a weak interaction [100]. The particle size was affected by the percentage of W; an average size of 9.3 nm was obtained with 1%, and when increasing to 5% the particle size was 11.9 nm. The increase in particle size is due to the variation of the surface charge density of the species generated from W at pH 3 where the surface is positively charged by the species HW₆O₂₁⁵⁻ [101] generating larger particles with 5% of W having a greater interaction between NiO and W [35].

M.Mafokoane found [36] that the addition of WO₃ changes the isoelectric point of the Al₂O₃ surface due to an increase in charge. They mentioned that the value of the isoelectric point of WO₃ and Al₂O₃ was 4.2 and 7.7 respectively; however, it was concluded that at higher loads WO₃(6%)-Al₂O₃ the isoelectric point presents a constant value, and this is because at higher loads of WO₃ forms a monolayer on alumina at pH > 6–7. Cruz-Perez et al. [102] revealed that the isoelectric point of the Al₂O₃-TiO₂ support is 6.0; however, this depended a lot on the preparation of the support. They described that at pH 4, adding W produces the ion W₁₂O₄₀⁸⁻ where Ni can be coordinated tetrahedrally and octahedrally. On the other hand, for a solution of W at pH 9, the ion W₁₂O₄₀⁸⁻ occurs, where Ni can be tetrahedrally coordinated. Even if the isoelectric point of Al₂O₃-TiO₂ is 6, it causes polymerization from the WO₄²⁻ monomer. According to the above, in the monometallic catalysts at pH 3, the Ni species with the increase in W can have a greater interaction with the support, coordinated tetrahedrally and octahedrally, as species NiAl₂O₄, which could cause a lower number of exposed metallic active sites, corroborating with the dispersion result seen in Table 4 and Figure 5 with TPD-H₂.

Figure 11a shows dispersed particles and small agglomerations on the surface of the support. The diffraction analysis of Figure 11b reveals the presence of the diffraction rings corresponding to Ni (111) and (220). In Figure 11c, planes corresponding to Ni (111) and (200) with interplanar distance of 0.203 nm and 0.176 nm, NiO (200) at 0.208 nm, and NiAl₂O₄ (111) and (411) were identified. The MET micrographs of the Ni/ATW5 B catalyst showed the dispersed and isolated particles on the surface of the support, which can be seen in Figure 12a. According to the diffraction analysis of the electron select area shown in Figure 12b, the phases of NiO (200), NiAl₂O₄ (440), Ni (111), and (200) were identified. Figure 12c reveals how metallic Ni grew in different directions of the plane (111) and (200) due to the reduction of NiO coming from the dehydration of the polycrystalline structure of Ni(OH)₂ that nucleates in different directions.

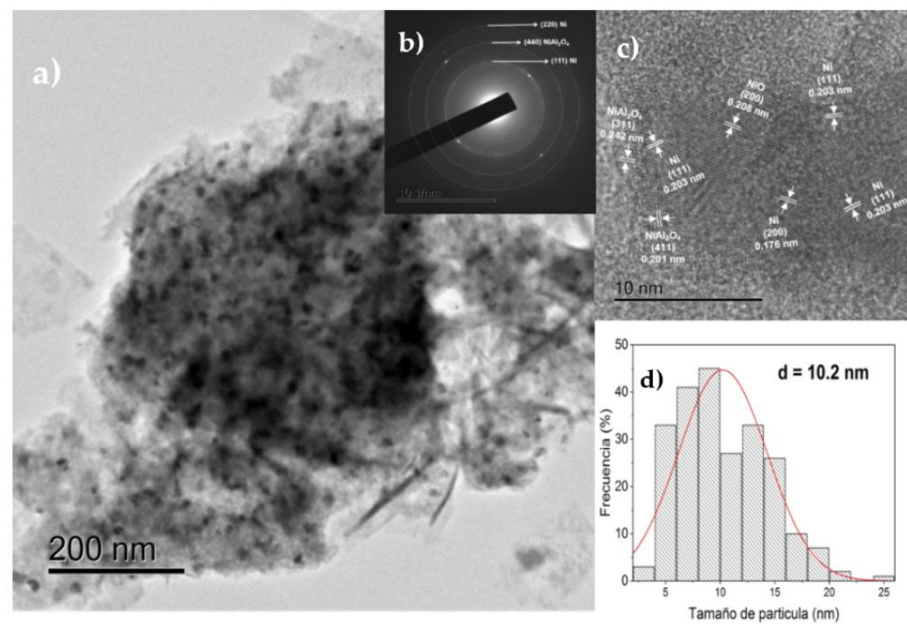


Figure 11. TEM pictures of the monometallic Ni/ATW1 B basic catalyst. (a) Particles of Ni on the surface of catalyst, (b) Electron diffraction patterns of Ni and NiAl₂O₄, (c) Interplanar distance measured of Ni⁰, NiO and NiAl₂O₄ and (d) Histogram distribution of metal particle size and average diameter of Ni.

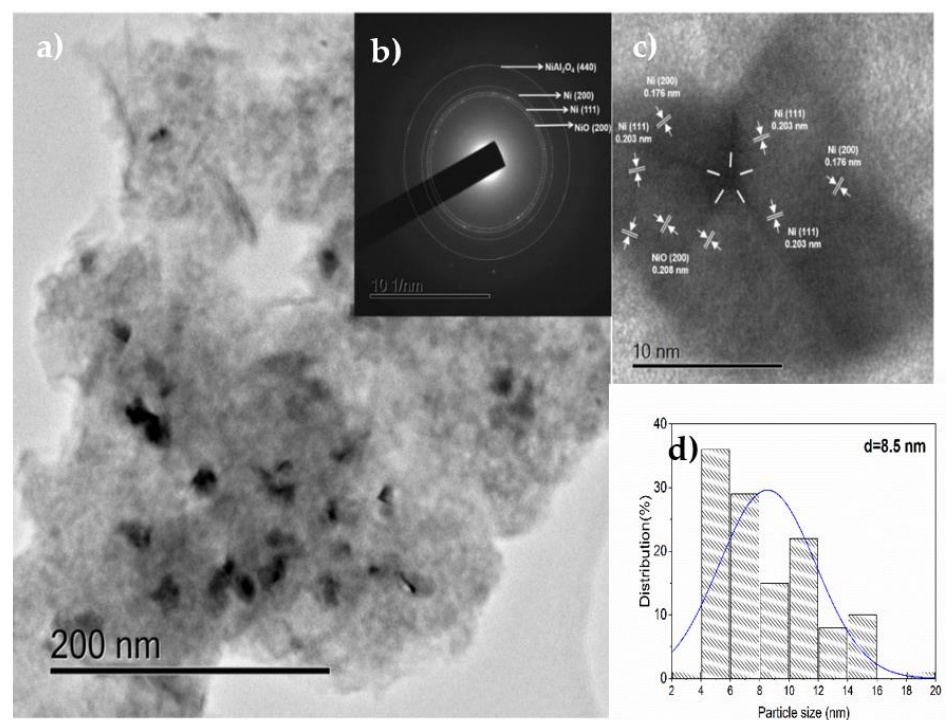


Figure 12. TEM pictures of the monometallic Ni/ATW5 B basic catalyst. (a) Particles of Ni on the surface of catalyst, (b) Electron diffraction patterns of Ni, NiO and NiAl₂O₄, (c) Interplanar distance measured of Ni⁰ and NiO and (d) Histogram distribution of metal particle size and average diameter of Ni.

The 0.176 nm interplanar distance was adapted to the plane (200) of Ni, which indicates that the Ni originated from the NiO matrix [99] dispersed by the increase in the percentage of WO₃, generating a better dispersion of nickel, and at the same time helping to inhibit the

formation of the NiAl_2O_4 spinel; although $\text{Al}_2(\text{WO}_4)_3$ was not identified in any catalyst, the XPS spectra, as discussed later, of the support suggest that there was an interaction of Al_2O_3 and WO_3 due to the displacement of binding energies of the O1s. In Figures 11d and 12d it is observed that as the percentage of W increased from 1% to 5%, the average crystallite size decreased from 10.2 nm to 8.5 nm. The modification of the support with W rises a better dispersion of Ni, contributing to a smaller particle size with 5% of W; the species of W at pH 9 could increase the negative charge on the surface of the support, improving the dispersion of the Ni^{2+} ions; the formation of $\text{Al}_2(\text{WO}_4)_3$ can prevent the diffusion of Ni^{2+} into the Al_2O_3 network.

3.1.8. FTIR-Pyridine

The results of the pyridine adsorption showed absorption bands of Lewis and Brønsted sites and are presented in the infrared region between 1700 and 1400 cm^{-1} corresponding to the absorbed pyridine [103].

Figure 13 shows the infrared spectra of all monometallic catalysts at $170\text{ }^\circ\text{C}$. The bands located at 1606 cm^{-1} , 1575 cm^{-1} , 1488 cm^{-1} , and 1447 cm^{-1} characteristic to the absorption of pyridines in Lewis-type acid centers were identified, which corresponded to the interaction of pair electrons of pyridine on the metal cations. The bands at 1485 , 1545 , and 1640 cm^{-1} from the Brønsted sites generated a PyH^+ protonation on pyridinium ion [103,104]; however, none of these bands were detected. The bands located at 1445 cm^{-1} and 1606 cm^{-1} corresponded to the ν_{19a} and ν_{8a} coordination respectively; this is attributed to the coordinated pyridine in hydrogen bonds in Lewis acid centers generated by Ni metal sites and by the support [105,106].

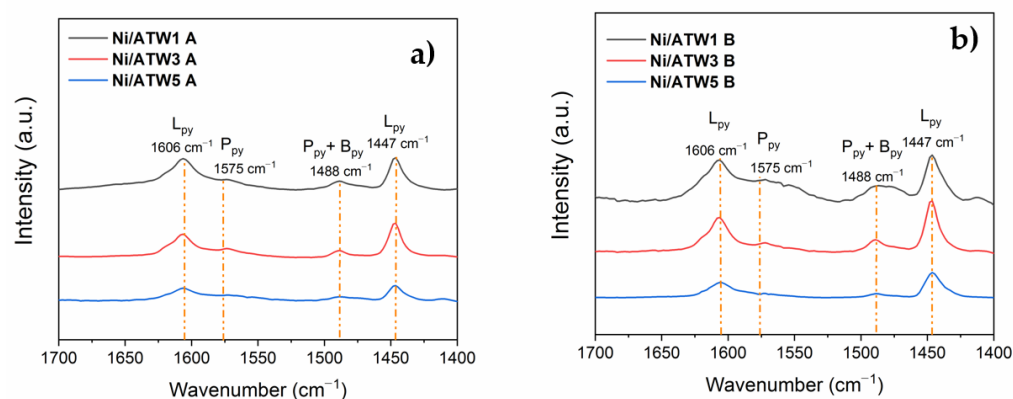


Figure 13. Pyridine FTIR spectrums at $170\text{ }^\circ\text{C}$ of the monometallic acid and basic catalysts (a) Ni/ATW A and (b) Ni/ATW B.

Increased Lewis acidity may be generated because of the $\text{W}=\text{O}$ bonds with unsaturated coordination of the W^{6+} species observed by both the Raman and FTIR spectra (not shown here). While, the bands at 1575 cm^{-1} with coordination ν_{19a} and 1488 cm^{-1} with coordination ν_{8a} correspond to weak Lewis's acid centers [104]. As stated by Leal et al. [106] and Mafokoane et al. [36] the band at 1488 cm^{-1} is typical of pyridine adsorbed at sites (Lewis + Brønsted); the absence of Brønsted sites located at 1540 cm^{-1} and 1640 cm^{-1} decreased due to the Ni charge from the ion exchange of the Brønsted sites for the positive charge of the Ni^{2+} species, which were unsaturated, causing Lewis sites [50]. This is due to the Al_2O_3 coating on the support according to Raman spectra (not shown here); Tanabe et al. [107,108] mentioned that Al_2O_3 only has Lewis acid sites, and this Lewis acidity is related to Al^{3+} cations in tetrahedral coordination [109]. The absence of the 1540 cm^{-1} band indicated that there were no Brønsted sites on the surface strong enough to react with pyridine at a temperature of $200\text{ }^\circ\text{C}$. The low intensity observed in Figure 13 of the monometallic catalysts could be due to the coating of Ni metallic particles in Lewis-type active centers. These

results are consistent with those presented by Jia et al. [76] where using Ni only promoted the presence of predominant Lewis sites on the surface of the monometallic catalyst.

The number of identified acidic sites were calculated by integrating the area under the curve. The results are shown in Table 4. The total number of Lewis sites was higher in the Ni/ATW B monometallic catalysts following this order: Ni/ATW1 B > Ni/ATW3 B > Ni/ATW5 B. The Ni/ATW1 B catalyst obtained higher Lewis acid sites. On the other hand, the Ni/ATW A catalysts preceded the following order of Lewis acid sites Ni/ATW3 A > Ni/ATW5 A > Ni/ATW1 A.

The increase in Lewis acid sites in the Ni/ATW3 A and Ni/ATW5 A catalyst is due to the low content of metallic Ni species, as a result of the incomplete reduction from the strong metal–support interaction because of the increase in W, generating the increase of Ni(OH)₂; the Ni species of the Ni/ATW5 A catalyst were found in NiAl₂O₄ and Ni(OH)₂ 2 as shown by the XPS spectra and the TPR profile. The increase in Lewis acid sites due to the increase in the W load could be caused by the increase in Ni(OH)₂ concentrations with the increase in W. The increase in the number of sites is evident with the increase in surface area when comparing the Ni/ATW1 A catalyst with Ni/ATW5 B catalyst; however, it can be given that the W species generated on the support at different synthesis pH values [95]. The density of Lewis acid sites $\mu\text{mol}/\text{m}^2$ in the Ni/ATW5 A catalyst was $0.89 \mu\text{mol}/\text{m}^2$, and it decreased with 5% of W due to the increase in the surface area with respect to the Ni/ATW1 A catalyst with an amount of acid sites of Lewis per m^2 of $0.84 \mu\text{mol}/\text{m}^2$. It was observed that higher Lewis acid sites were generated at pH 9, possibly due to the species $\text{W}_{12}\text{O}_{40}^{8-}$ and WO_4^{2-} [95,101] increasing the density of Lewis acid sites.

3.1.9. XPS

Figure 14 reveals Ni2p_{3/2} spectra of Ni/ATW catalysts. The broad Ni2p_{3/2} peak is associated with more than one nickel state. The presence of metallic nickel was identified in 852.4–852.6 eV and Ni²⁺ species, the latter presenting two types of interactions: one with the γ -Al₂O₃ and the other with the hydroxyl groups. The binding energy values as well as the percentage of the species are shown in Table 5. The existence of the Ni³⁺ species can be explained by the formation of a nickel spinel NiAl₂O₄ according to the energy values in 856.2–856.6 eV [110,111] as reported by Ruan and Zhang et al. [112,113]. On the other hand, the signal at 856 eV can be associated with the existence of Ni³⁺ species; therefore, the existence of three Ni species (Ni³⁺, Ni²⁺, and Ni⁰) can be seen. The interaction with the strong OH groups that remained on the surface after the reductive treatment resulted in the formation of nickel hydroxides Ni(OH)₂ [114].

Table 5. Binding energy (eV) of Ni2p_{3/2} of Ni⁰, Ni(OH)₂, and NiAl₂O₄ phases in monometallic Ni/AWTX A and Ni/AWTX B catalysts.

Catalyst	Binding Energy Ni2p _{3/2} (Ni ⁰) (eV)	Binding Energy Ni2p _{3/2} (Ni(OH) ₂) (eV)	Binding Energy Ni2p _{3/2} (NiAl ₂ O ₄) (eV)
Ni/ATW1 A	852.6 (9.2%)	855.5 (25.2%)	856.3 (65.6%)
Ni/ATW3 A	852.4 (8.2%)	855.4 (31.8%)	856.2 (60%)
Ni/ATW5 A	852.4 (7.3%)	855.3 (46.9%)	856.6 (45.8%)
Ni/ATW1 B	852.3 (7.2%)	855.3 (64.9%)	856.7 (27.8%)
Ni/ATW5 B	852.2 (10.1%)	855.2 (61.3%)	856.6 (28.6%)

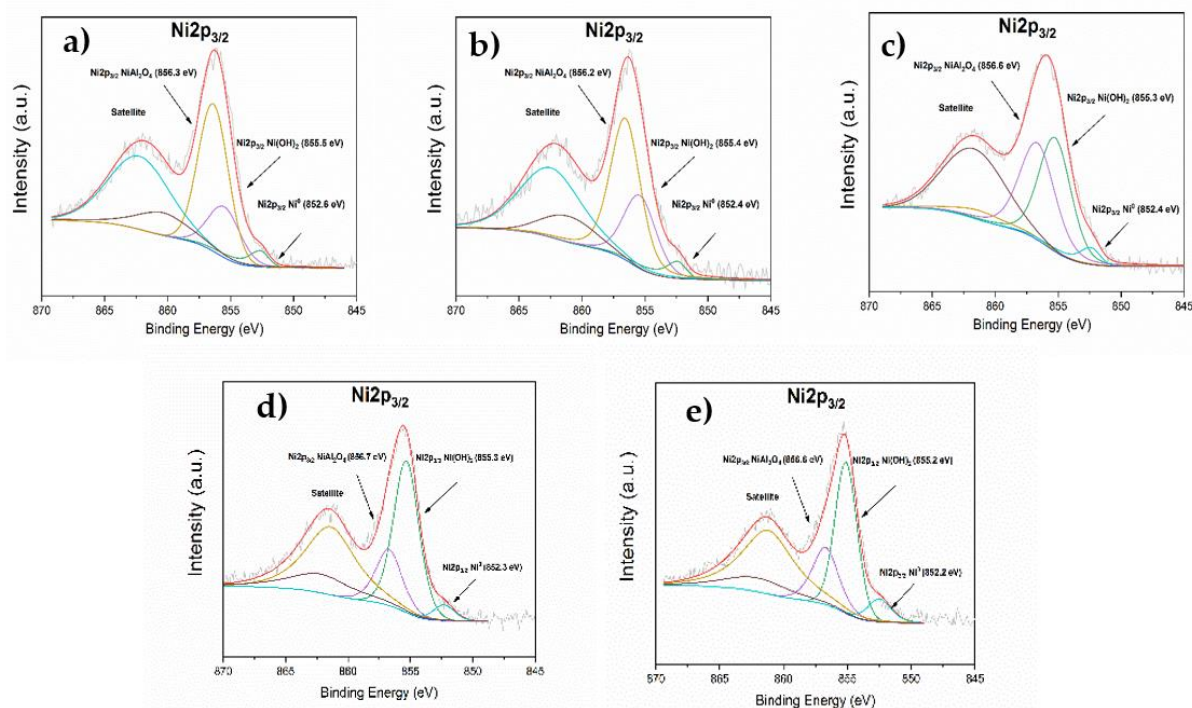


Figure 14. Ni $2p_{3/2}$ XPS spectra of the monometallic acid catalysts (a) Ni/ATW1 A, (b) Ni/ATW3 A, (c) Ni/ATW5 A, (d) Ni/ATW1 B, and (e) Ni/ATW5 B.

In Figure 14a–c it is observed how the Ni(OH) $_2$ species grows with the content of W; a binding energy shift of 855.5 eV with 1% of W up to 855.2 eV is observed, and this shift of 0.3 eV is given by interaction of Ni with W particles, which was also observed in the TPR-H $_2$ profiles, where reduction signals were detected at high temperatures with the increase of W to 5% *w/w*, suggesting the interaction of Ni particles with the W of the support [35]. It is possible that OH groups serve as a diffusion medium to interact within the aluminum matrix due to the wide peak at 856 eV, which may be due to the interaction of Ni $^{2+}$ and Ni $^{3+}$ species, occupying available tetrahedral and octahedral sites.

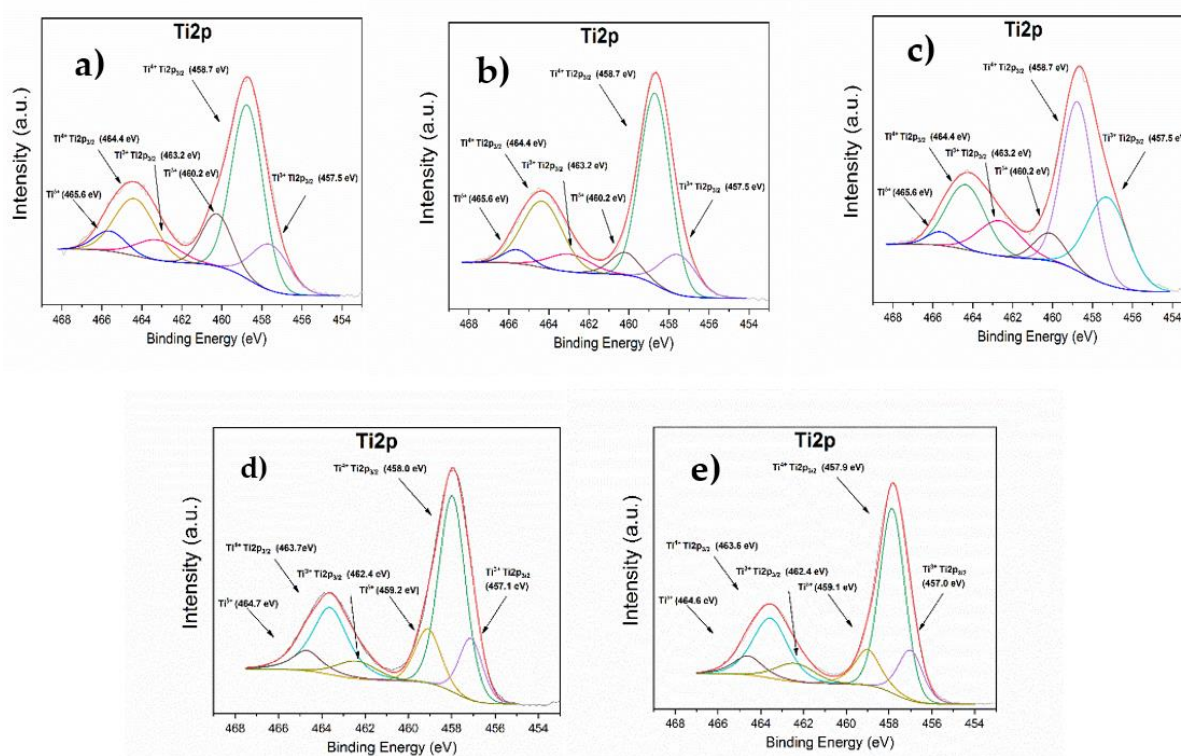
According to Q Zhang, the interaction of Ni $^{2+}$ species with alumina favors two species: NiO (with oxygen from the network) and Ni(OH) $_2$ (surface OH); Spanou et al. [97] mentioned that these species are formed mainly on the Ni/TiO $_2$ surface and they are characterized by being mostly reducible. On the other hand, they are more difficult to reduce when carried out in abundant areas of the γ -Al $_2$ O $_3$ phase, depending on the state of coordination being more difficult to reduce when they have octahedral coordination. The binding energies reported close to 856.5–857 eV correspond to Ni $2p_{3/2}$ in the NiAl $_2$ O $_4$ species [115]. Furthermore, the amplitude of the peak at 862 eV supports the presence of NiAl $_2$ O $_4$, according to the literature on nickel aluminates; these species present an inverted spinel, where the divalent Ni $^{2+}$ can occupy tetrahedral sites and the trivalent species, such as Ni $^{3+}$, octahedral sites. It has been reported [74] that this species is formed at temperatures of 500 °C; based on XPS analysis and X-ray diffraction, it is inferred that free NiO forms a layer on the surface of the support, which is more easily to reduce unlike NiO that is bound to γ -Al $_2$ O $_3$ sharing the same oxygen with aluminum.

Table 6 summarizes the values of the binding energies of the catalysts for Ti $2p_{2/3}$, W $4f_{7/2}$, Al $2p$, and O $1s$. In this table, slight changes in the binding energies are observed in the peak of W $4f_{7/2}$ as the percentage of W, in the support increases. The change in binding energies suggests that both WO $_3$ Al $_2$ O $_3$ and TiO $_2$ interacted by transferring electron density to WO $_3$, causing a decrease in the binding energy of W $4f$.

Table 6. Binding energy (eV) of $Ti_{2p_{3/2}}$, $W_{4f_{7/2}}$, Al_{2p} , and O_{1s} in monometallic Ni/ATW A and Ni/ATW B catalysts.

Catalyst	Binding Energy $Ti_{2p_{3/2}}$ (Ti^{4+}/Ti^{3+}) (eV)	Binding Energy $W_{4f_{7/2}}$ (W^{6+}) (eV)	Binding Energy Al_{2p} (Al^{3+} AlO_3/AlO_4) (eV)	Binding Energy O_{1s} (eV)
Ni/ATW1 A	458.7/457.5	35.7	74.6/73.5	531.6, 530.5, 529.6
Ni/ATW3 A	458.7/457.5	35.8	74.6/73.5	531.5, 530.5, 529.6
Ni/ATW5 A	458.7/457.5	35.4	74.6/73.5	531.6, 530.5, 529.6
Ni/ATW1 B	458.0/457.1	35.3	74.4/73.3	531.1, 530.1, 529.4
Ni/ATW5 B	457.9/457.0	35.2	74.2/73.3	531.1, 530.0, 529.3

The high-resolution Ti_{2p} spectra of the Ni/ATW monometallic catalysts are shown in Figure 15. The broad peak at 458 eV, which could be attributed to the existence of 2 oxidation states, is in contrast to pure TiO_2 according to the literature [116]. However, a broader peak is observed in the Ni/ATW5 A material, possibly due to the metal–support interaction considering the increase in the tungsten charge to 5%.

**Figure 15.** Ti_{2p} XPS spectra of the monometallic basic catalysts (a) Ni/ATW1 A, (b) Ni/ATW3 A, (c) Ni/ATW5 A, (d) Ni/ATW1 B, (e) Ni/ATW5 B.

The Ti_{2p} spectrum was analyzed using a Gaussian–Lawrencian curve with a Shirley background where a main peak was found at 458 eV, presenting a FWHM value higher than 2 eV, which indicates the existence of not only the Ti^{4+} species. Two doublets located at 458.7 eV and 464.3 eV that belong to the $Ti_{2p_{3/2}}-Ti_{2p_{1/2}}$ Ti^{4+} species were identified; according to the binding energy difference of 5.6 eV, the Anatase phase is confirmed [117,118].

The Ti^{4+} reduction was possible due to the presence of Ni; the dissociatively chemisorbed hydrogen in Ni can diffuse from the Ni surface to the support where in areas of TiO_2 can be reduced from Ti^{4+} to Ti^{3+} , this effect being mentioned by Riyapan and Xu et al. [119,120] using Pd/ TiO_2 where the reduction of Ti^{4+} was observed at a temperature below 450 °C due to the homolytic dissociation of H_2 on the support. This can generate the substitution of the W^{6+} ions in Ti^{4+} due to the close value of the ionic radius, as well as the interaction

of W^{6+} modifying the chemical environment of Al^{3+} , in its AlO_6 and AlO_4 coordination states in 74.6 eV and 73.5 eV as observed in Table 5.

All these factors contributed to the formation of Ti^{3+} species to compensate for charges generated by the elimination of hydroxyl groups, producing oxygen vacancies O^{2-} , and these binding energies are observed in Figure 15 at values of 457.4 eV and 462.6 eV belonging to the $Ti2p_{3/2}$ and $Ti2p_{1/2}$ species for Ti^{3+} . These charge transfers can leave deficient areas on the surface, originating unstabilized Ti^{3+} species that can be in an electron transfer flux with Ni^{3+} species; the peaks found at 460 eV and 465.6 eV would correspond to the binding energy of $Ti2p$ of Ni-Ti in the intermetallic state [121] with tetrahedral coordination [122].

The peaks located at 37.9 eV and 35.7 eV correspond to the binding energy $Wf_{47/2}$ and $Wf_{45/2}$ respectively, which are characteristic of the W^{6+} species [66]. The O1s peak of 531.5–531.6 eV is assigned to the OH and oxygen groups Al-O, easy to assign due to the difference in electronegativity of Al between the elements involved (Ti, W, Ni) and according to previous works [123]. As stated by Reddy et al. [124] there are O^{2-} vacancies generated during the synthesis method in a reducing atmosphere and in the γ - Al_2O_3 phase itself that help the dispersion of Ni^{2+} species because of these oxygen vacancies, where nickel coordinates at tetrahedral and/or octahedral sites. The peak at 530.5 eV belongs to the oxygen found in the network as a result of the contribution of the different elements, TiO_2 , WO_3 , and Al_2O_3 [117], according to the studies carried out by Benjaram M et al. [123]. The displacement to higher eV could be due to the chemical environment produced by the oxygen vacancies generated by H_2 treatment; these defects generate a negative charge deficit that is compensated by the decrease in positive charge, that is, forming Ti^{3+} ions which actually act as electron donors, and in turn, new Ti-O-W bonds are generated with WO_3 to stabilize the charges, demonstrating a decrease in the charge density on the Ti and Al atoms due to the bonding with WO_3 [123] with charges of less than 1 and 3% by weight of W. The peak at 529.6 eV is caused by the interaction of Ni^{2+} in tetrahedral sites creating bonds of Ni-O [125] that combine with oxygens within the $NiAl_2O_4$ spinel because of this strong interaction.

3.2. Conversion of Levulinic Acid (LA) to γ -Valerolactone (GVL)

3.2.1. Catalytic Activity of the ATW51 A

Figure 16 reveals the catalytic activity of support ATW1 A, which showed a conversion of 80% at 60 min of reaction; the conversion of LA increased until reaching 98% conversion in a reaction time of 240 min.

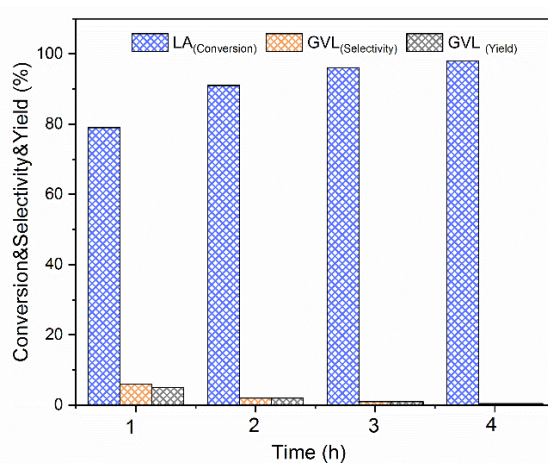


Figure 16. Results of the reaction using ATW1 A acid support. Reaction conditions: 4 MPa of H_2 pressure, rate of agitation of 500 rpm, 0.2 g of LA, 0.6 g cat, and temperature = 170 °C.

A 6% yield of GVL was obtained at 60 min. In general, the esterification of levulinic acid occurs in the presence of an alcohol such as methanol, ethanol, propanol, or butanol

with an acid catalyst [7,32,126]. The conversion of levulinic acid of 79% in 1 h suggested the formation of methyl levulinate due to methanol as a reaction medium that favors the reaction [32,48,50]. Enumula et al. [34] studied a W-SBA-16 system with 3% *w/w* of W where the Lewis and Brönsted type acidity increased in the support and surface area, improving levulinic acid conversions. Selectivity to ethyl levulinate is higher with 3% W, and there is no improvement in catalytic activity using 5%.

¹H-NMR of the Crude after Reaction

Figure 17a shows the ¹H-NMR spectrum of the ATW1A catalyst corresponding to the reaction crude after 2 h. There are strong signals of the esterification process of levulinic acid to methyl levulinate. The triplets generated by the neighboring CH₂ protons were detected in their corresponding carbons (#2CH₂, δ = 2.57 ppm and #3CH₂, δ = 2.76 ppm); additionally, the singlets for these protons (#5CH₃, δ = 2.19 ppm and #6CH₃, δ = 3.67 ppm) were noticed. Figure 17b shows the ¹H-NMR spectrum of a sample analyzed after 4 h of reaction. Signals of the protons of the conversion of Levulinic Acid were recognized (singlet #5CH₃, the triplets of the protons #2CH₂ and #3CH₂), methyl levulinate or methyl 4-oxopentanoate (singlets of the protons #5CH₃ and #6CH₃, the triplets of #2CH₂ and #3CH₂ protons), Methyl 4-Hydroxypentanoate (#5CH₃, #6CH₃ protons singlets, #2CH₂, #3CH₂ protons triplets and a #4CH proton signal multiplet), and γ-Valerolactone generated the multiplicity of neighboring protons for #3CH₂ and #4CH₂ multiplicity of #5CH, and finally the doublet corresponding to #6CH₃ developed from its neighbor CH. These results are very important because the conversion of levulinic acid into reaction by-products such as esters can be monitored, where acidic sites are needed and, in the hydrogenation process, it is required to have available active metal sites on the catalyst surface to produce γ-Valerolactone.

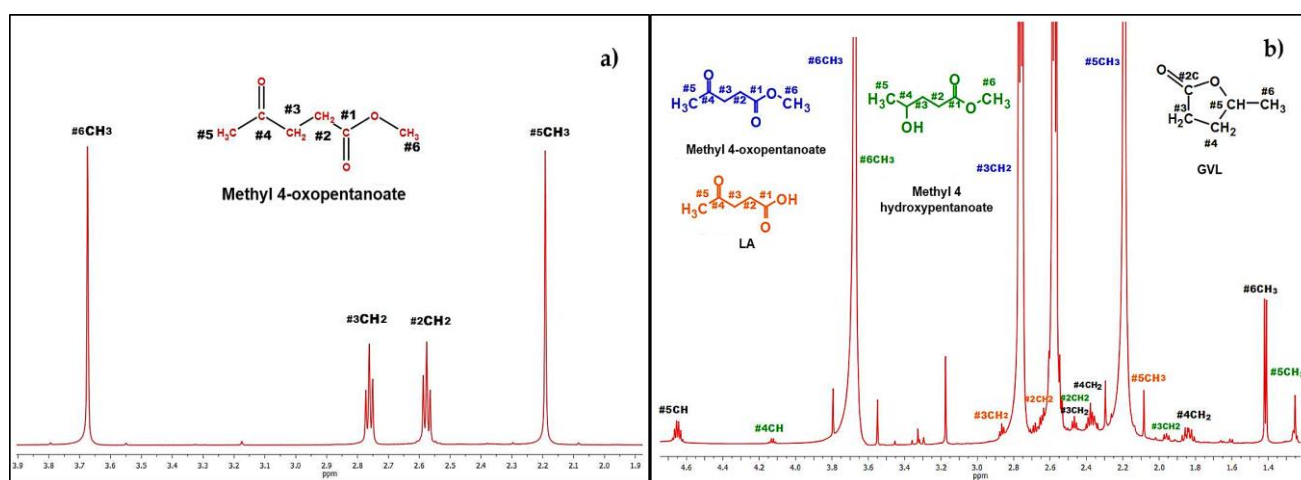


Figure 17. H1-NMR spectra of the reaction crude of levulinic acid (LA) to γ -Valerolactone reaction using ATW1A acid support after (a) 2 h of the reaction and (b) 4 h of the reaction.

3.3. Catalytic Tests of the Ni/ATW Catalysts

Figure 18 shows the results of the monometallic catalysts at different times. The yields decrease when the % of W increases, and this is due to: (a) the decomposition of levulinic acid by the Ti³⁺ species generating a carbon deposit on the surface resulting in lower yields or (b) by the adsorption of water molecules released by esterification or by physisorbed water from the support. Pham et al. [127] mentioned that the Ti³⁺ species cause the decomposition of levulinic acid because the ketone group of levulinic acid binds preferentially to these Ti sites and they are coordinately unsaturated through the carbonyl oxygen atom, so despite from the high conversion of levulinic acid, the yield of GVL decreases; these results are similar to those presented by the group of Mafokoane et al. [36].

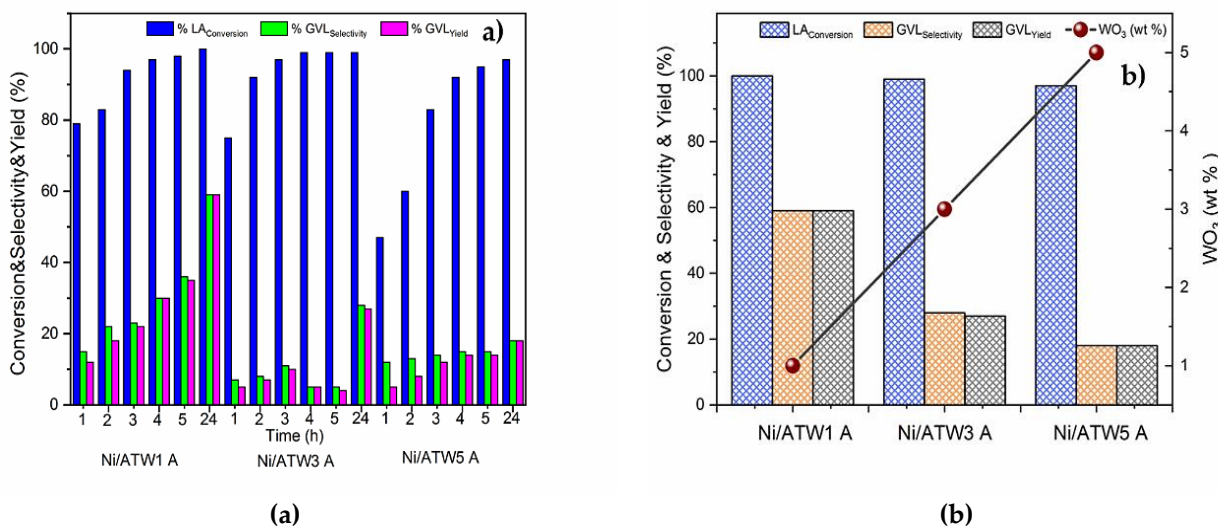


Figure 18. Results of the reaction of LA to GVL using methanol and Ni/ATW1 A, Ni/ATW3 A, and Ni/ATW5 A monometallic catalysts on acid supports synthesized at pH 3 using acetic acid (CH₃COOH). (a) Conversion, selectivity, and yield at different times of the reaction and (b) effect of the WO₃ load in the conversion, selectivity, and yield at 24 h of the reaction.

On the other hand, the 24 h GVL yield of the Ni/ATW B catalysts in Figure 19 showed the following trend: Ni/ATW5 B > Ni/ATW3 B > Ni/ATW1 B (see Table 7). From the results of the IR spectra of pyridine it can be observed that, while the amount of Lewis sites decreased, the yield of GVL increased; in addition, the increase in surface area causes a better dispersion of the Ni particles, and this indicates that the average pore diameter increased due to the fact that the ATW support was modified at pH 9 using NH₄OH, which could have helped the Ni deposit within the pores because the W species generated dispersed more efficiently the Ni in the support at pH 9 with NH₄OH, and it was also observed that as the W load increased, the GVL performance increased.

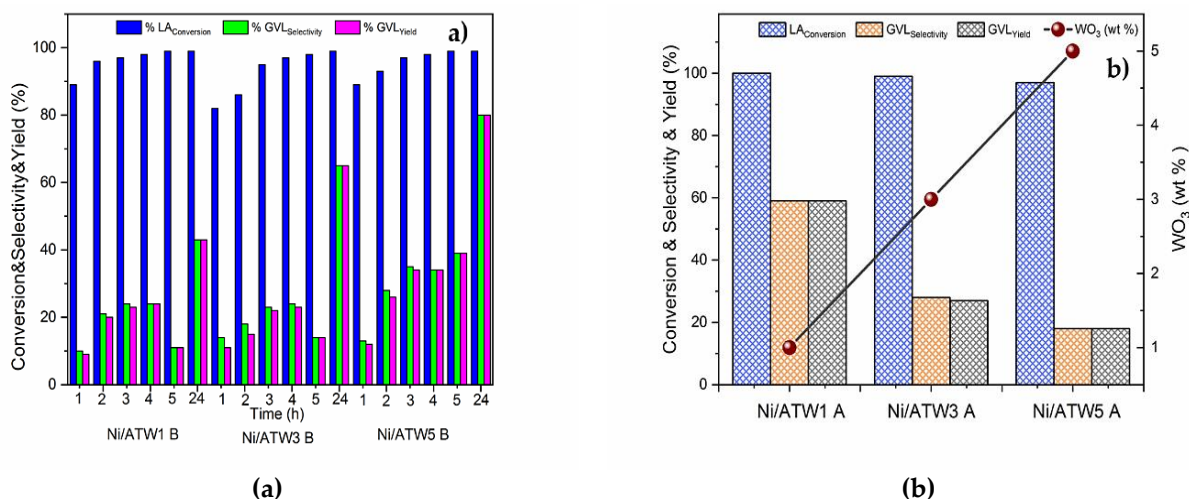


Figure 19. Results of the reaction of LA to GVL using methanol and Ni/ATW1 B, Ni/ATW3 B and Ni/ATW5 B monometallic catalysts on basic supports synthesized at pH 9 using ammonium hydroxide (NH₄OH). (a) Conversion, selectivity, and yield at different times of the reaction and (b) effect of the WO₃ load in the conversion, selectivity, and yield at 24 h of the reaction.

Table 7. Conversion and Yield of LA hydrogenation to GVL, using ATW A support and monometallic Ni/ATWX acid and basic.

Catalyst	LA Conversion (%)	GVL Yield (%)
ATW1 A	100	6 ^a
Ni/ATW1 A	100	59
Ni/ATW3 A	100	27
Ni/ATW5 A	97	18
Ni/ATW1 B	100	43
Ni/ATW3 B	100	65
Ni/ATW5 B	100	80

Reaction conditions: 4 MPa of H₂ pressure, 500 rpm agitation rate, 0.2 g of LA, 0.6 g cat, and 170 °C. a: Time of the reaction 1 hr.

3.3.1. ¹H-NMR Elucidation by Products

For this Ni/ATW1 A nickel monometallic catalyst (See Figure 20), methyl levulinate signals were elucidated by finding the characteristic triplets generated by the vicinal CH₂ with their displacements for each proton (#2CH₂, δ = 2.55 ppm and #3CH₂, δ = 2.78 ppm); a singlet was observed for the methyls (#5CH₃, δ = 2.19 ppm) and (#6CH₃, δ = 3.70 ppm). In the case of the GVL, the multiplicity of the neighboring protons were generated for (#4CH₂ δ = 1.88 ppm and 2.38 ppm) and (#3CH₂ δ = 2.45 ppm), the multiplicity of (CH, δ = 4.66 ppm), and finally the doublet (CH₃, δ = 1.41 ppm) generated from its neighbor CH [128]. The strong signals for methyl levulinate correspond to the excess percentage.

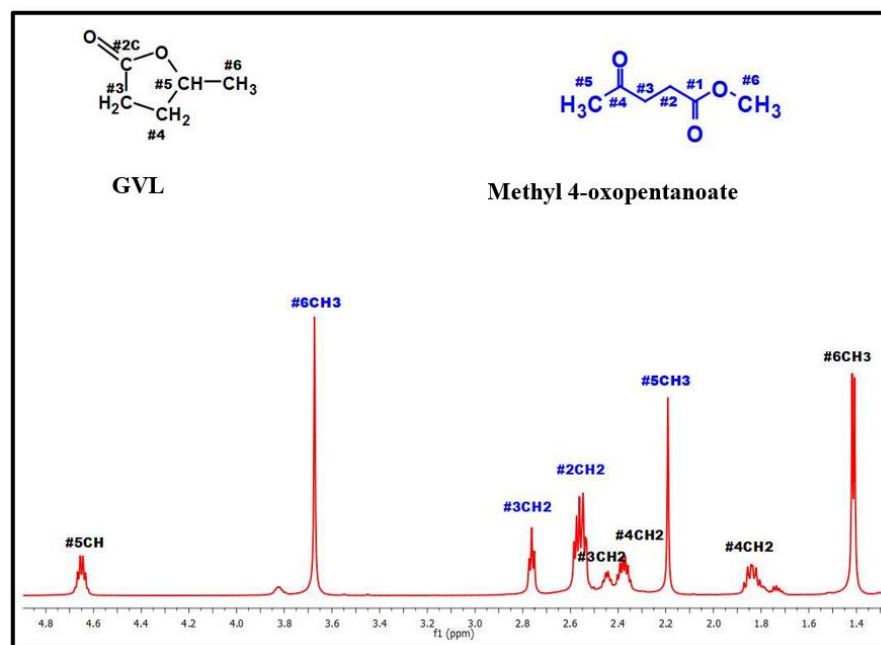


Figure 20. ¹H-NMR spectra (CDCl₃) of the crude after reaction using Ni/ATW1 A acid catalyst in Levulinic Acid (LA) to γ -Valerolactone after 24 h of the reaction.

The different reaction routes are shown in Figure 21. GVL's poor performance is due to competition from sites; Lewis sites were generated by the support and by Ni²⁺ species in the form of NiO, Ni(OH)₂ and NiAl₂O₄, first promoting esterification, forming Methyl-Levulinate, and subsequently being hydrogenated by metallic sites. At the same time, according to the results obtained by ¹H-NMR, LA is hydrogenated to form 4-hydroxypentanoic acid. The existence of Lewis sites that provides the catalyst monometallic catalysts promotes the esterification of LA to methyl-levulinate; simultaneously, LA is hydrogenated to 4-hydroxypentanoic acid due to the metallic sites, and subsequently

GVL is obtained. However, considering the medium of reaction in methanol and the competition of Lewis sites, the esterification of Levulinic Acid (LA) and the conversion of 4-hydroxypentanoic acid to GVL need to be minimal in the first hours of reaction.

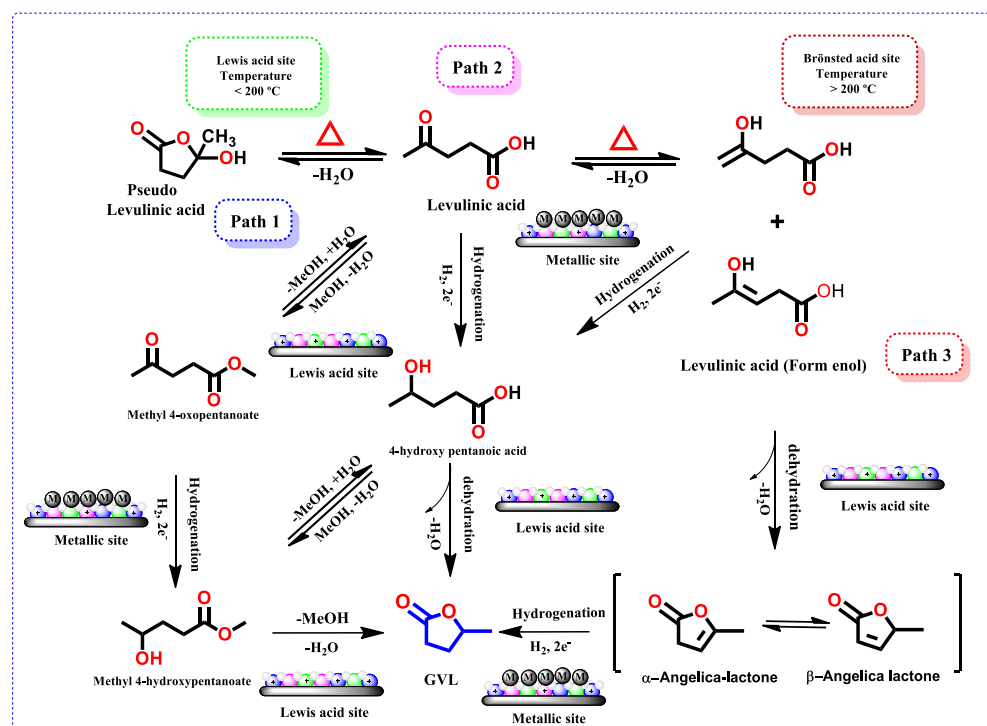


Figure 21. γ -Valerolactone paths of the formation from LA [7,14,15,26,32,48,129,130].

Therefore, at 24 h when 100% conversion of Levulinic Acid has been reached, there is no competition from metallic sites for the hydrogenation of Levulinic Acid; therefore, the hydrogenation of methyl levulinate is more selective to form methyl 4-hydroxypentanoate so that later dehydration by Lewis sites can take place and finally intramolecular dealcoholization, forming γ -Valerolactone.

3.3.2. Effect of Lewis Acid Sites on the Yield to GVL

The increase in Lewis acid sites (see Table 4) did not affect the conversion of Levulinic Acid for the Ni/ATW1 A catalysts; for Ni/ATW3 B it was 100% and 97% for the Ni/ATW5 A catalyst (see Figure 22 and Table 7). The maximum conversion of GVL was obtained with 1% of WO_3 of the Ni/ATW1 A catalyst with 59% (see Table 7) with $207.9 \mu\text{mol}/\text{g}_{\text{cat}}$. When 1% increases to 3% the Lewis acid sites increased up to $428.9 \mu\text{mol}/\text{g}_{\text{cat}}$, decreasing the GVL yield up to 27% (see Table 7), and the conversion to GVL lowered the selectivity with the increase in the Lewis acid sites. It is expected that the Ni/ATW5 A catalyst with $246 \mu\text{mol}/\text{g}_{\text{cat}}$ increased the GVL yield; however, a GVL yield of 18% (see Table 7) was obtained, and this could be due to the increase in surface area and the increase in Ti^{3+} species because the increase in 5% of WO_3 . Although the yields decreased with the increase of WO_3 in the support, the reaction was not selective to α -angelica lactone, but rather followed the route of the esterification of Levulinic Acid. These results suggest that with an excess of Lewis acid sites the yield of GVL decreases, generating the decomposition of Levulinic Acid and limiting the conversion to methyl levulinate, lowering the selectivity to GVL. For Ni/ATW B catalysts, the maximum GVL yield was obtained with 5% of WO_3 and Ni/ATW5 B catalyst with 80% with $385.9 \mu\text{mol}/\text{g}_{\text{cat}}$. The Lewis acid sites increased to $445.9 \mu\text{mol}/\text{g}_{\text{cat}}$ with 3% of WO_3 , decreasing the GVL yield to 65% for the catalyst with 1% of WO_3 the amount of Lewis acid sites was $458.9 \mu\text{mol}/\text{g}_{\text{cat}}$; under this system, the maximum acidity was found using only 1% of WO_3 , though it is clear that the conversion

to GVL decreases with the increase in Lewis acid sites. It was expected that the GVL performance of Ni/ATW1 B catalyst would be like the Ni/ATW3 B catalyst since the number of basic sites is alike, but it did not follow that trend, and this may be due to the WO_3 species that were found on the surface, generating dispersion of the Ni nanoparticles. The effect of NH_4OH influences the Ni deposition and the OH groups favor the dispersion of Ni, improving the yield of GVL.

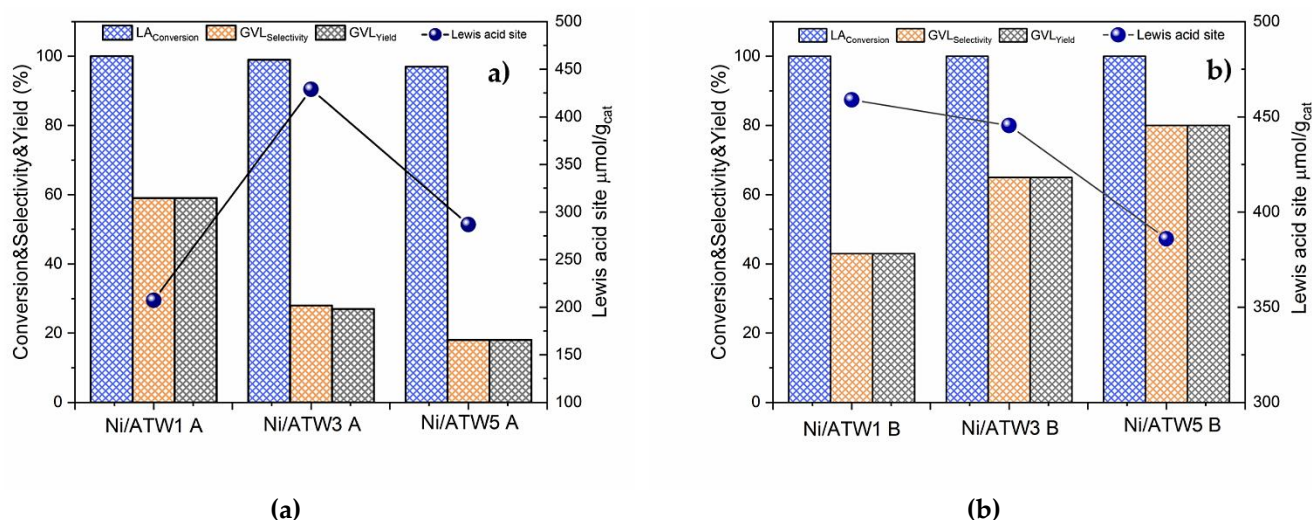


Figure 22. Effect of the Lewis acid sites on the monometallic catalysts in the GVL production. (a) Ni/ATWX A acid catalysts and (b) Ni/ATWX B basic catalysts.

3.3.3. Effect of the Ni Particle Size on the Yield to GVL

In Figure 23a, it is observed how the particle size influences the GVL yield after 24 h of reaction. A yield of 59% of GVL was obtained when the particle size was 9.2 nm (TEM, see Table 4) in the Ni/ATW1 A catalyst, and the formation of small particles with a low W load (1% *w/w*) was favored; with 5% *w/w* of W, the particle size increased to 11.9 nm (TEM, see Table 4), affecting the GVL yield by only obtaining 18% in the Ni/ATW5 A catalyst. These results show the influence of the particle size in the selectivity to GVL, the low nickel content helping in the generation of particles smaller than 10 nm [46]; however, the dispersion and the interaction with the support can modify the particle size due to a greater metal–support interaction [35,43]. It was studied how the particle size, the percentage of nickel, and the amount of Lewis acid sites show a favorable synergistic effect to have a yield at GVL. According to the results, when there is a high percentage of nickel, the particle size is greater than 10 nm, affecting the performance at GVL. Small nickel particles showed higher activity due to higher Ni surface area or due to higher reactivity of less coordinated sites. It is interesting to note that when the particle size was smaller with 1% W in the Ni/ATW1 A catalyst, there was a greater amount of NiAl_2O_4 , which suggests the existence of Ni^{2+} and Ni^{3+} species acting as Lewis sites, responsible for levulinic acid adsorption and the activation of the carbonyl group of the carboxylic acid in the small particles of metallic nickel [34,131]. As reported by Song [132], the adsorption of H_2 would take place on Ni (111) and levulinic acid on NiO (111). Diffusion of H_2 species occurs through hydroxyl groups [133]; the synergy of support and metal sites is necessary for efficient hydrogenation of levulinic acid to GVL.

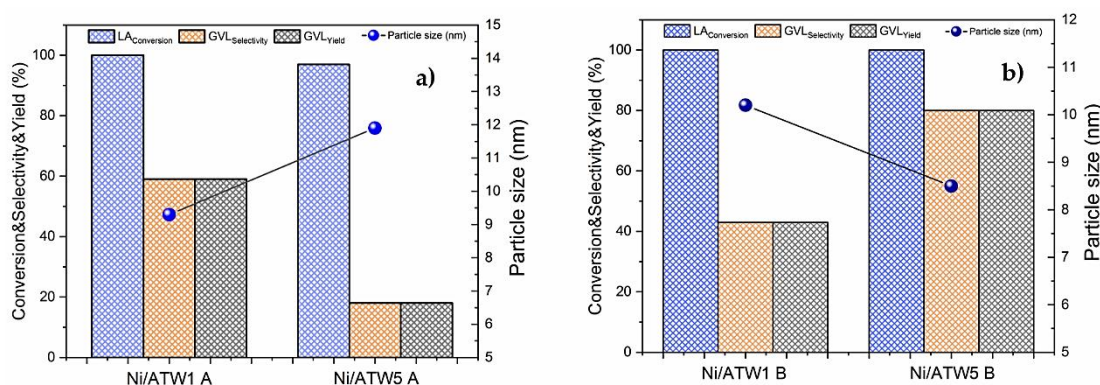


Figure 23. Effect of the particle size of the catalysts in the conversion, selectivity, and yield of the LA to GVL. (a) Ni/ATWX A acid catalysts and (b) Ni/ATWX B basic catalysts.

The particle size obtained by TEM is compared with the yield of GVL in Figure 23b. The Ni/ATW5 B catalyst showed a higher performance, the improvement in these results being caused by the particle size of 8.5 nm (TEM, see Table 4) compared with the Ni/ATW1 B catalyst because the spillover effect is carried out in small particles, dissociating the H₂. The presence of OH groups is important in this type of reaction, since they function as H₂ transport, so the Ni(OH)₂ species as well as M-OH groups in the support serve as a diffusion medium. Cheng et al. [134] reported that it is likely that this effect depends equally on the acidity of the support and the synthesis method of the catalyst. Meith et al. [135] mentioned that when a pH of 5 is used, the predominant species are Ni²⁺, however at a pH greater than 6.5 these species transform into Ni(OH)₂, increasing the complexity of the system. Therefore, in the support at pH 9, the surface OH groups of the support generate a better dispersion of the Ni²⁺ species when they exchange with the OH groups forming Ni(OH)₂, and these species in presence of molecular H₂ due to the spillover effect can reduce nickel in situ by increasing metallic sites. When the OH groups decrease, the nickel begins to nucleate on and around the already fixed metal sites [136], growing the particle size and diminishing the yields of GVL.

3.3.4. Effect of de Ni⁰ Metallic Sites on the Yield to GVL

The results obtained in this research work suggested that the yield towards GVL decreases with an excess of Lewis acid sites, generating the decomposition of levulinic acid limiting the conversion to methyl levulinate, lowering the yield to GVL. However, the yield to GVL did not increase for the Ni/ATW5 A catalyst, although the Lewis acid sites were as the Ni/ATW1 A catalyst. This suggests that a necessary contribution of metallic sites with the Lewis acid sites is needed to have a high yield, the low yield of GVL is not only a function of the Lewis acid sites, but also of the percentage of metallic Ni. Figure 24 shows how the GVL performance is a function of the percentage of metallic Ni. Since the Ni/ATW1 A catalyst contains more metal sites 9.1%, H₂ can be dissociated in a homolytic way more effectively and by spillover effect, and H₂ is transported by OH groups [79,133]. Nonetheless, it is possible that when diffusing in the support it reduces NiO in situ, Ni(OH)₂ and NiAl₂O₄ species close to metallic Ni particles. In the TEM images, the interplanar distances of NiO, Ni(OH)₂, and NiAl₂O₄ within the limits of metallic Ni were observed, which would lead to a consumption of H₂ due to the reduction of these species, limiting the hydrogenation of levulinic acid or methyl levulinate, obtaining low yields in the first hours of reaction and a maximum yield at 24 h of reaction because of the generation of new active sites by the spillover effect.

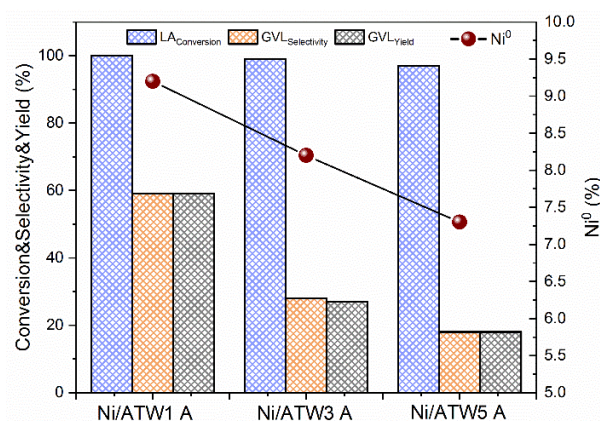


Figure 24. Effect of the Ni⁰ percentage in the conversion, selectivity and yield of LA to GVL reaction using monometallic Ni/ATW1 A, Ni/ATW3 A and Ni/ATW5 A acid catalysts.

4. Conclusions

The aim of this work was the modification of the Al₂O₃-TiO₂-WO₃ support using different pH of synthesis with different percentages of W and Ni at 10% by weight by the suspension method and its application in obtaining GVL from LA using methanol as solvent. The nickel particles dispersed adequately in the support, and the surface area as well as the volume and the pore diameter decreased once the nickel was deposited. All the catalysts showed a complete conversion of LA, this due to the esterification to methyl levulinate according to the results of ¹H-NMR. The high selectivity of esterification was attributed to the Lewis acid sites that all catalysts exhibited. The low percentage of metallic Ni could indicate the contribution of Lewis sites due to the presence of NiAl₂O₄ and Ni(OH)₂ species. Among all the catalysts prepared, the Ni/ATW5 B catalyst at pH 9 using 10% Ni and 5% *w/w* of W, in the support, showed the highest yield towards GVL, 80% at 24 h of reaction and 4 MPa of H₂ pressure; this suggests, according to TEM studies, that the catalytic activity is optimal at a smaller particle size. This was related to the W species generated at different pH of synthesis on the support that influenced the Ni particle size. The yield to GVL increased as the W amount in the support increased. These results suggest that the increase in W, in the support at pH 9, improves the stability of the Ni metallic particles, which leads to electronic and structural changes between the active phase (Ni metallic) and the Lewis acid sites, generating esterification from LA to methyl levulinate and increasing the yield to GVL by the spillover effect. However, when the Ni catalyst is supported on a modified support at pH 3, the generation of the species reduction from Ti⁴⁺ to Ti³⁺ is promoted, causing a decrease in the yield to GVL.

Author Contributions: Methodology, software, validation, formal analysis, investigation, writing—original draft, writing—review and editing, visualization, G.E.C.-P.; methodology, software, validation, formal analysis, investigation, writing—original draft, writing—review and editing, visualization, J.C.-E.; methodology, software, validation, formal analysis, investigation, writing—original draft, writing—review and editing, visualization, A.A.S.-P.; methodology, validation, investigation, writing—original draft, writing—review and editing, visualization, A.C.-U.; methodology, validation, investigation, writing—original draft, writing—review and editing, visualization, J.C.A.-P.; methodology, validation, investigation, writing—original draft, writing—review and editing, visualization, A.C.-G.; investigation, writing—original draft, writing—review and editing, visualization, A.E.E.d.l.M.; investigation, writing—original draft, writing—review and editing, visualization, C.G.E.-G.; investigation, writing—original draft, writing—review and editing, visualization, S.G.; investigation, writing—original draft, writing—review and editing, visualization, F.O.-C.; investigation, writing—original draft, writing—review and editing, Z.G.-Q.; conceptualization, methodology, validation, formal analysis, investigation, resources, writing—original draft, writing—review and editing, visualization, supervision, project administration, funding acquisition, J.G.T.-T. All authors have read and agreed to the published version of the manuscript.

Funding: This research was funded by National Council of Science and Technology (CONACYT) Scholarship number 730270, Project No. 132648, Project Number 1024 and SEP-PFCE-UJAT-DACB program project 2019–2020.

Institutional Review Board Statement: Not applicable.

Informed Consent Statement: Not applicable.

Data Availability Statement: Not applicable.

Acknowledgments: Gerardo Enrique Cordova Pérez sincerely thanks the National Council of Science and Technology for the scholarship granted (number 730270) to study the PhD in Materials Science within the graduate program of the Autonomous Juárez University of Tabasco. We would like to thank the National Council of Science and Technology (CONACYT), Project No. 132648, Cátedras CONACYT (Investigadoras e Investigadores por México) Project Number 1024 “Nanomaterials Study to Energy Applications” and finally the SEP-PFCE-UJAT-DACB program project for their financial support. We thank Karla M. Diaz Torres for the English support in this manuscript.

Conflicts of Interest: The authors declare no conflict of interest.

References

1. Climent, M.J.; Corma, A.; Iborra, S. Conversion of biomass platform molecules into fuel additives and liquid hydrocarbon fuels. *Green Chem.* **2014**, *16*, 516–547. [[CrossRef](#)]
2. Ragauskas, A.J.; Williams, C.K.; Davison, B.H.; Britovsek, G.; Cairney, J.; Eckert, C.A.; Frederick, W.J.; Hallett, J.P.; Leak, D.J.; Liotta, C.L.; et al. The Path Forward for Biofuels and Biomaterials. *Science* **2006**, *311*, 484–489. [[CrossRef](#)] [[PubMed](#)]
3. Mascal, M.; Dutta, S.; Wu, L. Preparation of Compounds from Levulinic Acid. Patent WO/2016/123459, 2020.
4. Werpy, T.; Petersen, G. *Top Value Added Chemicals from Biomass: Volume I—Results of Screening for Potential Candidates from Sugars and Synthesis Gas*; DOE/GO-102004-1992; TRN: US200427%671 United States 10.2172/15008859 TRN: US200427%671 NREL English; p. Medium: ED; National Renewable Energy Lab.: Golden, CO, USA, 2004; 76p.
5. Tulchinsky, M.L.; Briggs, J.R. One-Pot Synthesis of Alkyl 4-Alkoxy-pentanoates by Esterification and Reductive Etherification of Levulinic Acid in Alcoholic Solutions. *ACS Sustain. Chem. Eng.* **2016**, *4*, 4089–4093. [[CrossRef](#)]
6. Flores-Velázquez, V.; Córdova-Pérez, G.E.; Silahua-Pavón, A.A.; Torres-Torres, J.G.; Sierra, U.; Fernández, S.; Godavarthi, S.; Ortiz-Chi, F.; Espinosa-González, C.G. Cellulose obtained from banana plant waste for catalytic production of 5-HMF: Effect of grinding on the cellulose properties. *Fuel* **2020**, *265*, 116857. [[CrossRef](#)]
7. Xu, R.; Liu, K.; Du, H.; Liu, H.; Cao, X.; Zhao, X.; Qu, G.; Li, X.; Li, B.; Si, C. Falling Leaves Return to Their Roots: A Review on the Preparation of γ -Valerolactone from Lignocellulose and Its Application in the Conversion of Lignocellulose. *ChemSusChem* **2020**, *13*, 6461–6476. [[CrossRef](#)]
8. Hayes, D.; Fitzpatrick, S.; Hayes, M.; Ross, J. The Biofine Process@ Production of Levulinic Acid, Furfural, and Formic Acid from Lignocellulosic Feedstocks. *Biorefin. Ind. Processes Prod.* **2006**, *1*, 139–164.
9. Morales, G.; Melero, J.A.; Iglesias, J.; Paniagua, M.; López-Aguado, C. From levulinic acid biorefineries to γ -valerolactone (GVL) using a bi-functional Zr-Al-Beta catalyst. *React. Chem. Eng.* **2019**, *4*, 1834–1843. [[CrossRef](#)]
10. Alonso, D.M.; Wettstein, S.G.; Dumesic, J.A. Gamma-valerolactone, a sustainable platform molecule derived from lignocellulosic biomass. *Green Chem.* **2013**, *15*, 584–595. [[CrossRef](#)]
11. Tang, X.; Sun, Y.; Zeng, X.; Lei, T.; Li, H.; Lin, L. Chapter 7— γ -Valerolactone—an excellent solvent and a promising building block. In *Biomass, Biofuels, Biochemicals*; Saravanamurugan, S., Pandey, A., Li, H., Riisager, A., Eds.; Elsevier: Amsterdam, The Netherlands, 2020; pp. 199–226.
12. Osatiashtiani, A.; Lee, A.F.; Wilson, K. Recent advances in the production of γ -valerolactone from biomass-derived feedstocks via heterogeneous catalytic transfer hydrogenation. *J. Chem. Technol. Biotechnol.* **2017**, *92*, 1125–1135. [[CrossRef](#)]
13. Zhang, Z. Synthesis of γ -Valerolactone from Carbohydrates and its Applications. *ChemSusChem* **2016**, *9*, 156–171. [[CrossRef](#)]
14. Yu, Z.; Lu, X.; Xiong, J.; Ji, N. Transformation of Levulinic Acid to Valeric Biofuels: A Review on Heterogeneous Bifunctional Catalytic Systems. *ChemSusChem* **2019**, *12*, 3915–3930. [[CrossRef](#)] [[PubMed](#)]
15. Yu, Z.; Lu, X.; Bai, H.; Xiong, J.; Feng, W.; Ji, N. Effects of Solid Acid Supports on the Bifunctional Catalysis of Levulinic Acid to γ -Valerolactone: Catalytic Activity and Stability. *Chem. Asian J.* **2020**, *15*, 1182–1201. [[CrossRef](#)] [[PubMed](#)]
16. Horváth, I.T.; Mehdi, H.; Fábos, V.; Boda, L.; Mika, L.T. γ -Valerolactone—A sustainable liquid for energy and carbon-based chemicals. *Green Chem.* **2008**, *10*, 238–242. [[CrossRef](#)]
17. Bruno, T.J.; Wolk, A.; Naydich, A. Composition-Explicit Distillation Curves for Mixtures of Gasoline with Four-Carbon Alcohols (Butanols). *Energy Fuels* **2009**, *23*, 2295–2306. [[CrossRef](#)]
18. Wang, R.; Chen, L.; Zhang, X.; Zhang, Q.; Li, Y.; Wang, C.; Ma, L. Conversion of levulinic acid to γ -valerolactone over Ru/Al₂O₃-TiO₂ catalyst under mild conditions. *RSC Adv.* **2018**, *8*, 40989–40995. [[CrossRef](#)]

19. Zhang, Y.; Chen, C.; Gong, W.; Song, J.; Zhang, H.; Zhang, Y.; Wang, G.; Zhao, H. Self-assembled Pd/CeO₂ catalysts by a facile redox approach for high-efficiency hydrogenation of levulinic acid into gamma-valerolactone. *Catal. Commun.* **2017**, *93*, 10–14. [[CrossRef](#)]
20. Mustafin, K.; Cárdenas-Lizana, F.; Keane, M.A. Continuous gas phase catalytic transformation of levulinic acid to γ -valerolactone over supported Au catalysts. *J. Chem. Technol. Biotechnol.* **2017**, *92*, 2221–2228. [[CrossRef](#)]
21. Nemanashi, M.; Noh, J.-H.; Meijboom, R. Hydrogenation of biomass-derived levulinic acid to γ -valerolactone catalyzed by mesoporous supported dendrimer-derived Ru and Pt catalysts: An alternative method for the production of renewable biofuels. *Appl. Catal. A Gen.* **2018**, *550*, 77–89. [[CrossRef](#)]
22. Wang, J.; Wang, Y.; Tong, X.; Wang, Y.; Jin, G.; Guo, X. Highly active Ir/SiC catalyst for aqueous hydrogenation of levulinic acid to γ -valerolactone. *Catal. Commun.* **2020**, *139*, 105971. [[CrossRef](#)]
23. Upare, P.P.; Lee, J.-M.; Hwang, D.W.; Halligudi, S.B.; Hwang, Y.K.; Chang, J.-S. Selective hydrogenation of levulinic acid to γ -valerolactone over carbon-supported noble metal catalysts. *J. Ind. Eng. Chem.* **2011**, *17*, 287–292. [[CrossRef](#)]
24. Yan, Z.-P.; Lin, L.; Liu, S. Synthesis of γ -Valerolactone by Hydrogenation of Biomass-derived Levulinic Acid over Ru/C Catalyst. *Energy Fuels* **2009**, *23*, 3853–3858. [[CrossRef](#)]
25. Lange, J.-P.; Price, R.; Ayoub, P.M.; Louis, J.; Petrus, L.; Clarke, L.; Gosselink, H. Valeric Biofuels: A Platform of Cellulosic Transportation Fuels. *Angew. Chem. Int. Ed.* **2010**, *49*, 4479–4483. [[CrossRef](#)] [[PubMed](#)]
26. Malleshamb, B.; Sudarsanam, P.; Venkata Shiva Reddy, B.; Govinda Rao, B.; Reddy, B.M. Nanostructured Nickel/Silica Catalysts for Continuous Flow Conversion of Levulinic Acid to γ -Valerolactone. *ACS Omega* **2018**, *3*, 16839–16849. [[CrossRef](#)] [[PubMed](#)]
27. Fu, J.; Sheng, D.; Lu, X. Hydrogenation of Levulinic Acid over Nickel Catalysts Supported on Aluminum Oxide to Prepare γ -Valerolactone. *Catalysts* **2016**, *6*, 6. [[CrossRef](#)]
28. Stickney, J.A.; Sager, S.L.; Clarkson, J.R.; Smith, L.A.; Locey, B.J.; Bock, M.J.; Hartung, R.; Olp, S.F. An updated evaluation of the carcinogenic potential of 1,4-dioxane. *Regul. Toxicol. Pharmacol.* **2003**, *38*, 183–195. [[CrossRef](#)]
29. Jiang, K.; Sheng, D.; Zhang, Z.; Fu, J.; Hou, Z.; Lu, X. Hydrogenation of levulinic acid to γ -valerolactone in dioxane over mixed MgO–Al₂O₃ supported Ni catalyst. *Catal. Today* **2016**, *274*, 55–59. [[CrossRef](#)]
30. Lv, J.; Rong, Z.; Wang, Y.; Xiu, J.; Wang, Y.; Qu, J. Highly efficient conversion of biomass-derived levulinic acid into γ -valerolactone over Ni/MgO catalyst. *RSC Adv.* **2015**, *5*, 72037–72045. [[CrossRef](#)]
31. Hengne, A.M.; Kadu, B.S.; Biradar, N.S.; Chikate, R.C.; Rode, C.V. Transfer hydrogenation of biomass-derived levulinic acid to γ -valerolactone over supported Ni catalysts. *RSC Adv.* **2016**, *6*, 59753–59761. [[CrossRef](#)]
32. Hengne, A.M.; Rode, C.V. Cu–ZrO₂ nanocomposite catalyst for selective hydrogenation of levulinic acid and its ester to γ -valerolactone. *Green Chem.* **2012**, *14*, 1064–1072. [[CrossRef](#)]
33. Al-Shaal, M.G.; Wright, W.R.H.; Palkovits, R. Exploring the ruthenium catalysed synthesis of γ -valerolactone in alcohols and utilisation of mild solvent-free reaction conditions. *Green Chem.* **2012**, *14*, 1260–1263. [[CrossRef](#)]
34. Enumula, S.S.; Gurram, V.R.B.; Chada, R.R.; Burri, D.R.; Kamaraju, S.R.R. Clean synthesis of alkyl levulinates from levulinic acid over one pot synthesized WO₃–SBA-16 catalyst. *J. Mol. Catal. A Chem.* **2017**, *426*, 30–38. [[CrossRef](#)]
35. Kumar, V.V.; Naresh, G.; Deepa, S.; Bhavani, P.G.; Nagaraju, M.; Sudhakar, M.; Chary, K.V.R.; Tardio, J.; Bhargava, S.K.; Venugopal, A. Influence of W on the reduction behaviour and Brønsted acidity of Ni/TiO₂ catalyst in the hydrogenation of levulinic acid to valeric acid: Pyridine adsorbed DRIFTS study. *Appl. Catal. A Gen.* **2017**, *531*, 169–176. [[CrossRef](#)]
36. Mafokoane, M.; Seguel, J.; García, R.; Díaz de León, J.N.; Sepúlveda, C.; Escalona, N. Conversion of levulinic acid using CuO/WO₃(x)-Al₂O₃ catalysts. *Catal. Today* **2020**, *367*, 310–319. [[CrossRef](#)]
37. Yuan, L.; Guo, S.; Li, Z.; Cui, H.; Dong, H.; Zhao, L.; Wang, J. Ring opening of decalin over bifunctional Ni–W carbide/Al₂O₃–USY catalysts and monofunctional acid Ni–W oxide/Al₂O₃–USY. *RSC Adv.* **2017**, *7*, 9446–9455. [[CrossRef](#)]
38. Luo, W.; Deka, U.; Beale, A.M.; van Eck, E.R.H.; Bruijninx, P.C.A.; Weckhuysen, B.M. Ruthenium-catalyzed hydrogenation of levulinic acid: Influence of the support and solvent on catalyst selectivity and stability. *J. Catal.* **2013**, *301*, 175–186. [[CrossRef](#)]
39. Mohan, V.; Venkateswarlu, V.; Pramod, C.V.; Raju, B.D.; Rao, K.S.R. Vapour phase hydrocyclisation of levulinic acid to γ -valerolactone over supported Ni catalysts. *Catal. Sci. Technol.* **2014**, *4*, 1253–1259. [[CrossRef](#)]
40. Enumula, S.S.; Gurram, V.R.B.; Kondeboina, M.; Burri, D.R.; Kamaraju, S.R.R. ZrO₂/SBA-15 as an efficient catalyst for the production of γ -valerolactone from biomass-derived levulinic acid in the vapour phase at atmospheric pressure. *RSC Adv.* **2016**, *6*, 20230–20239. [[CrossRef](#)]
41. Shokrollahi Yancheshmeh, M.; Alizadeh Sahraei, O.; Aissaoui, M.; Iliuta, M.C. A novel synthesis of NiAl₂O₄ spinel from a Ni–Al mixed-metal alkoxide as a highly efficient catalyst for hydrogen production by glycerol steam reforming. *Appl. Catal. B Environ.* **2020**, *265*, 118535. [[CrossRef](#)]
42. Zhang, Q.; Wu, T.; Zhang, P.; Qi, R.; Huang, R.; Song, X.; Gao, L. Facile synthesis of hollow hierarchical Ni/ γ -Al₂O₃ nanocomposites for methane dry reforming catalysis. *RSC Adv.* **2014**, *4*, 51184–51193. [[CrossRef](#)]
43. Hengst, K.; Ligthart, D.A.J.M.; Doronkin, D.E.; Walter, K.M.; Kleist, W.; Hensen, E.J.M.; Grunwaldt, J.-D. Continuous Synthesis of γ -Valerolactone in a Trickle-Bed Reactor over Supported Nickel Catalysts. *Ind. Eng. Chem. Res.* **2017**, *56*, 2680–2689. [[CrossRef](#)]
44. Kondeboina, M.; Enumula, S.S.; Reddy, K.S.; Challa, P.; Burri, D.R.; Kamaraju, S.R.R. Bimetallic Ni–Co/ γ -Al₂O₃ catalyst for vapour phase production of γ -valerolactone: Deactivation studies and feedstock selection. *Fuel* **2021**, *285*, 119094. [[CrossRef](#)]
45. Primo, A.; Concepción, P.; Corma, A. Synergy between the metal nanoparticles and the support for the hydrogenation of functionalized carboxylic acids to diols on Ru/TiO₂. *Chem. Commun.* **2011**, *47*, 3613–3615. [[CrossRef](#)] [[PubMed](#)]

46. Dutta, S.; Yu, I.K.M.; Tsang, D.C.W.; Ng, Y.H.; Ok, Y.S.; Sherwood, J.; Clark, J.H. Green synthesis of gamma-valerolactone (GVL) through hydrogenation of biomass-derived levulinic acid using non-noble metal catalysts: A critical review. *Chem. Eng. J.* **2019**, *372*, 992–1006. [[CrossRef](#)]
47. Hengst, K.; Schubert, M.; Carvalho, H.W.P.; Lu, C.; Kleist, W.; Grunwaldt, J.-D. Synthesis of γ -valerolactone by hydrogenation of levulinic acid over supported nickel catalysts. *Appl. Catal. A Gen.* **2015**, *502*, 18–26. [[CrossRef](#)]
48. Sudhakar, M.; Kumar, V.V.; Naresh, G.; Kantam, M.L.; Bhargava, S.K.; Venugopal, A. Vapor phase hydrogenation of aqueous levulinic acid over hydroxyapatite supported metal (M = Pd, Pt, Ru, Cu, Ni) catalysts. *Appl. Catal. B Environ.* **2016**, *180*, 113–120. [[CrossRef](#)]
49. Kumar, V.V.; Naresh, G.; Sudhakar, M.; Tardio, J.; Bhargava, S.K.; Venugopal, A. Role of Brønsted and Lewis acid sites on Ni/TiO₂ catalyst for vapour phase hydrogenation of levulinic acid: Kinetic and mechanistic study. *Appl. Catal. A Gen.* **2015**, *505*, 217–223. [[CrossRef](#)]
50. Singh, H.; Iyengar, N.; Yadav, R.; Rai, A.; Sinha, A.K. Facile conversion of levulinic acid to γ -valerolactone using a high surface area magnetically separable Ni/NiO catalyst. *Sustain. Energy Fuels* **2018**, *2*, 1699–1706. [[CrossRef](#)]
51. Shimizu, K.-I.; Kanno, S.; Kon, K. Hydrogenation of levulinic acid to γ -valerolactone by Ni and MoO_x co-loaded carbon catalysts. *Green Chem.* **2014**, *16*, 3899–3903. [[CrossRef](#)]
52. Sun, D.; Ohkubo, A.; Asami, K.; Katori, T.; Yamada, Y.; Sato, S. Vapor-phase hydrogenation of levulinic acid and methyl levulinate to γ -valerolactone over non-noble metal-based catalysts. *Mol. Catal.* **2017**, *437*, 105–113. [[CrossRef](#)]
53. Atanda, L.; Silahua, A.; Mukundan, S.; Shrotri, A.; Torres-Torres, G.; Beltramini, J. Catalytic behaviour of TiO₂-ZrO₂ binary oxide synthesized by sol-gel process for glucose conversion to 5-hydroxymethylfurfural. *RSC Adv.* **2015**, *5*, 80346–80352. [[CrossRef](#)]
54. Silahua-Pavón, A.A.; Espinosa-González, C.G.; Ortiz-Chi, F.; Pacheco-Sosa, J.G.; Pérez-Vidal, H.; Arévalo-Pérez, J.C.; Godavarthi, S.; Torres-Torres, J.G. Production of 5-HMF from glucose using TiO₂-ZrO₂ catalysts: Effect of the sol-gel synthesis additive. *Catal. Commun.* **2019**, *129*, 105723. [[CrossRef](#)]
55. Córdova-Pérez, G.E.; Torres-Torres, G.; Ortíz-Chi, F.; Godavarthi, S.; Silahua-Pavón, A.A.; Izquierdo-Colorado, A.; Da Costa, P.; Hernández-Como, N.; Aleman, M.; Espinosa-González, C.G. Effect of Acid-Basic Sites Ratio on the Catalytic Activity to Obtain 5-HMF from Glucose Using Al₂O₃-TiO₂-W Catalysts. *ChemistrySelect* **2018**, *3*, 12854–12864. [[CrossRef](#)]
56. Guo, J.; Zhu, S.; Cen, Y.; Qin, Z.; Wang, J.; Fan, W. Ordered mesoporous Nb-W oxides for the conversion of glucose to fructose, mannose and 5-hydroxymethylfurfural. *Appl. Catal. B Environ.* **2017**, *200*, 611–619. [[CrossRef](#)]
57. Kwak, J.H.; Mei, D.; Peden, C.H.F.; Rousseau, R.; Szanyi, J. (100) facets of γ -Al₂O₃: The Active Surfaces for Alcohol Dehydration Reactions. *Catal. Lett.* **2011**, *141*, 649–655. [[CrossRef](#)]
58. Hengne, A.; Biradar, N.; Rode, C. Surface species of supported ruthenium catalysts in selective hydrogenation of levulinic esters for bio-refinery application. *Catal. Lett.* **2012**, *142*, 779–787. [[CrossRef](#)]
59. Cortez-Elizalde, J.; Cuauhtémoc-López, I.; Guerra-Que, Z.; Espinosa de los Monteros, A.E.; Lunagómez-Rocha, M.A.; Silahua-Pavón, A.A.; Arévalo-Pérez, J.C.; Cordero-García, A.; Cervantes-Urbe, A.; Torres-Torres, J.G. Chemical and Structural Changes by Gold Addition Using Recharge Method in NiW/Al₂O₃-CeO₂-TiO₂ Nanomaterials. *Materials* **2021**, *14*, 5470. [[CrossRef](#)]
60. Tao, F.; Yang, S.; Yang, P.; Shi, Z.; Zhou, R. Effects of support property on the catalytic performance of CeO₂-ZrO₂-CrO_x for 1,2-dichloroethane oxidation. *J. Rare Earths* **2016**, *34*, 381–389. [[CrossRef](#)]
61. Rodríguez-Martínez, C.; García-Domínguez, Á.E.; Guerrero-Robles, F.; Saavedra-Díaz, R.O.; Torres-Torres, G.; Felipe, C.; Ojeda-López, R.; Silahua-Pavón, A.; Cervantes-Urbe, A. Synthesis of Supported Metal Nanoparticles (Au/TiO₂) by the Suspension Impregnation Method. *J. Compos. Sci.* **2020**, *4*, 89. [[CrossRef](#)]
62. Thommes, M.; Kaneko, K.; Neimark, A.V.; Olivier, J.P.; Rodriguez-Reinoso, F.; Rouquerol, J.; Sing, K.S. Physisorption of gases, with special reference to the evaluation of surface area and pore size distribution (IUPAC Technical Report). *Pure Appl. Chem.* **2015**, *87*, 1051–1069. [[CrossRef](#)]
63. Benoit, A.; Paramasivam, I.; Nah, Y.C.; Roy, P.; Schmuki, P. Decoration of TiO₂ nanotube layers with WO₃ nanocrystals for high-electrochromic activity. *Electrochem. Commun.* **2009**, *11*, 728–732. [[CrossRef](#)]
64. Mohrhusen, L.; Al-Shamery, K. Conversion of methanol on rutile TiO₂ (110) and tungsten oxide clusters: 1. population of defect-dependent thermal reaction pathways. *Phys. Chem. Chem. Phys.* **2021**, *23*, 12137–12147. [[CrossRef](#)]
65. Kuo, I.J.; Suzuki, N.; Yamauchi, Y.; Wu, K.C.W. Cellulose-to-HMF conversion using crystalline mesoporous titania and zirconia nanocatalysts in ionic liquid systems. *RSC Adv.* **2013**, *3*, 2028–2034. [[CrossRef](#)]
66. Zhao, F.; Yi, L.; Deng, R.; You, K.; Song, J.; Jian, J.; Liu, P.; Ai, Q.; Luo, H.A. Supported WO₃/ γ -Al₂O₃ as bifunctional catalyst for liquid-phase highly selective oxidation of cyclohexylamine to cyclohexanone oxime under solvent-free conditions. *Mol. Catal.* **2019**, *475*, 110494. [[CrossRef](#)]
67. Wang, C.; Li, Y.; Qiu, P.; Duan, L.; Bi, W.; Chen, Y.; Guo, D.; Liu, Y.; Luo, W.; Deng, Y. Controllable synthesis of highly crystallized mesoporous TiO₂/WO₃ heterojunctions for acetone gas sensing. *Chin. Chem. Lett.* **2020**, *31*, 1119–1123. [[CrossRef](#)]
68. Escobar, J.; De los Reyes, J.A.; Viveros, T. Influence of the Synthesis Additive on the Textural and Structural Characteristics of Sol-Gel Al₂O₃-TiO₂. *Ind. Eng. Chem. Res.* **2000**, *39*, 666–672. [[CrossRef](#)]
69. Li, Y.; Wu, L.; Wang, Y.; Ke, P.; Xu, J.; Guan, B. γ -Al₂O₃ doped with cerium to enhance electron transfer in catalytic ozonation of phenol. *J. Water Process Eng.* **2020**, *36*, 101313. [[CrossRef](#)]
70. Zou, X.; Rui, Z.; Song, S.; Ji, H. Enhanced methane combustion performance over NiAl₂O₄-interface-promoted Pd/ γ -Al₂O₃. *J. Catal.* **2016**, *338*, 192–201. [[CrossRef](#)]

71. Calvo, M.; Jiménez González, C.; Rivas, B.; Gutiérrez-Ortiz, J.; Lopez-Fonseca, R. Effect of Ni/Al molar ratio on the performance of substoichiometric NiAl₂O₄ spinel-based catalysts for partial oxidation of methane. *Appl. Catal. B Environ.* **2017**, *209*, 128–138. [[CrossRef](#)]
72. Ragupathi, C.; Vijaya, J.J.; Kennedy, L.J. Preparation, characterization and catalytic properties of nickel aluminate nanoparticles: A comparison between conventional and microwave method. *J. Saudi Chem. Soc.* **2017**, *21*, S231–S239. [[CrossRef](#)]
73. Escobar, J.; De los Reyes, J.; Viveros-García, T. Nickel on TiO₂-modified Al₂O₃ sol–gel oxides: Effect of synthesis parameters on the supported phase properties. *Appl. Catal. A Gen.* **2003**, *253*, 151–163. [[CrossRef](#)]
74. Gullapelli, S.; Scurrrell, M.S.; Valluri, D.K. Photocatalytic H₂ production from glycerol–water mixtures over Ni/γ-Al₂O₃ and TiO₂ composite systems. *Int. J. Hydrogen Energy* **2017**, *42*, 15031–15043. [[CrossRef](#)]
75. Gholami, T.; Salavati-Niasari, M.; Varshoy, S. Electrochemical hydrogen storage capacity and optical properties of NiAl₂O₄/NiO nanocomposite synthesized by green method. *Int. J. Hydrogen Energy* **2017**, *42*, 5235–5245. [[CrossRef](#)]
76. Jia, W.; Chen, Y.; Liu, M.; Liu, X.; Liu, X.; Yuan, J.; Lu, X.; Zhu, Z. Effect of calcination temperature and fluorination treatment on NiF₂-AlF₃ catalysts for dehydrofluorination of 1, 1, 1, 2-tetrafluoroethane to synthesize trifluoroethylene. *Appl. Catal. A Gen.* **2018**, *571*, 150–157. [[CrossRef](#)]
77. Zurita-Mendez, N.N.; Carbajal-De la Torre, G.; Cadenas, E.; Liu, H.; Espinosa-Medina, M.A. Synthesis and characterization of nickel aluminate nanoparticles. *Mater. Res. Express* **2018**, *6*, 015036. [[CrossRef](#)]
78. Scheffer, B.; Heijeinga, J.J.; Mouljn, J.A. An electron spectroscopy and x-ray diffraction study of nickel oxide/alumina and nickel-oxide-tungsten trioxide/alumina catalysts. *J. Phys. Chem.* **1987**, *91*, 4752–4759. [[CrossRef](#)]
79. Prins, R. Hydrogen Spillover. Facts and Fiction. *Chem. Rev.* **2012**, *112*, 2714–2738. [[CrossRef](#)]
80. Xu, Y.; Wu, S.; Wan, P.; Sun, J.; Hood, Z.D. Introducing Ti³⁺ defects based on lattice distortion for enhanced visible light photoreactivity in TiO₂ microspheres. *RSC Adv.* **2017**, *7*, 32461–32467. [[CrossRef](#)]
81. Ewbank, J.L.; Kovarik, L.; Diallo, F.Z.; Sievers, C. Effect of metal–support interactions in Ni/Al₂O₃ catalysts with low metal loading for methane dry reforming. *Appl. Catal. A Gen.* **2015**, *494*, 57–67. [[CrossRef](#)]
82. Zieliński, J. Morphology of nickel/alumina catalysts. *J. Catal.* **1982**, *76*, 157–163. [[CrossRef](#)]
83. Gao, J.; Jia, C.; Li, J.; Zhang, M.; Gu, F.; Xu, G.; Zhong, Z.; Su, F. Ni/Al₂O₃ catalysts for CO methanation: Effect of Al₂O₃ supports calcined at different temperatures. *J. Energy Chem.* **2013**, *22*, 919–927. [[CrossRef](#)]
84. Kumar, V.V.; Naresh, G.; Sudhakar, M.; Anjaneyulu, C.; Bhargava, S.K.; Tardio, J.; Reddy, V.K.; Padmasri, A.H.; Venugopal, A. An investigation on the influence of support type for Ni catalysed vapour phase hydrogenation of aqueous levulinic acid to γ-valerolactone. *RSC Adv.* **2016**, *6*, 9872–9879. [[CrossRef](#)]
85. Yang, R.; Du, X.; Zhang, X.; Xin, H.; Zhou, K.; Li, D.; Hu, C. Transformation of Jatropha Oil into High-Quality Biofuel over Ni–W Bimetallic Catalysts. *ACS Omega* **2019**, *4*, 10580–10592. [[CrossRef](#)] [[PubMed](#)]
86. Lin, W.; Cheng, H.; He, L.; Yu, Y.; Zhao, F. High performance of Ir-promoted Ni/TiO₂ catalyst toward the selective hydrogenation of cinnamaldehyde. *J. Catal.* **2013**, *303*, 110–116. [[CrossRef](#)]
87. Hinojosa-Reyes, M.; Rodríguez-González, V.; Zanella, R. Gold nanoparticles supported on TiO₂–Ni as catalysts for hydrogen purification via water–Gas shift reaction. *RSC Adv.* **2014**, *4*, 4308–4316. [[CrossRef](#)]
88. Mihet, M.; Lazar, M.D. Effect of Pd and Rh promotion on Ni/Al₂O₃ for NO reduction by hydrogen for stationary applications. *Chem. Eng. J.* **2014**, *251*, 310–318. [[CrossRef](#)]
89. Zeng, Y.; Ma, H.; Zhang, H.; Ying, W.; Fang, D. Highly efficient NiAl₂O₄-free Ni/γ-Al₂O₃ catalysts prepared by solution combustion method for CO methanation. *Fuel* **2014**, *137*, 155–163. [[CrossRef](#)]
90. Jordão, M.H.; Assaf, J.M.; Nascente, P.A.P. Surface Characterization of W/Ni/Al₂O₃ Catalysts. *MRS Proc.* **2011**, *497*, 243. [[CrossRef](#)]
91. Horsley, J.A.; Wachs, I.E.; Brown, J.M.; Via, G.H.; Hardcastle, F.D. Structure of surface tungsten oxide species in the tungsten trioxide/alumina supported oxide system from x-ray absorption near-edge spectroscopy and Raman spectroscopy. *J. Phys. Chem.* **1987**, *91*, 4014–4020. [[CrossRef](#)]
92. Yan, X.; Yuan, C.; Bao, J.; Li, S.; Qi, D.; Wang, Q.; Zhao, B.; Hu, T.; Fan, L.; Fan, B.; et al. A Ni-based catalyst with enhanced Ni–support interaction for highly efficient CO methanation. *Catal. Sci. Technol.* **2018**, *8*, 3474–3483. [[CrossRef](#)]
93. Chary, K.V.R.; Ramana Rao, P.V.; Venkat Rao, V. Catalytic functionalities of nickel supported on different polymorphs of alumina. *Catal. Commun.* **2008**, *9*, 886–893. [[CrossRef](#)]
94. Crisóstomo, C.A.B.; Almeida, T.S.S.; Soares, R.R. Towards triglycerides-based biorefineries: Hydrolysis-reforming-hydrogenation in one-pot over Ni/γ-Al₂O₃ based catalysts. *Catal. Today* **2020**, *367*, 124–136. [[CrossRef](#)]
95. Díaz de León, J.N.; Picquart, M.; Villarroel, M.; Vrinat, M.; Gil Llambias, F.J.; Murrieta, F.; de los Reyes, J.A. Effect of gallium as an additive in hydrodesulfurization WS₂/γ-Al₂O₃ catalysts. *J. Mol. Catal. A Chem.* **2010**, *323*, 1–6. [[CrossRef](#)]
96. Liao, M.; Wang, C.; Bu, E.; Chen, Y.; Cheng, Z.; Luo, X.; Shu, R.; Wu, J. Efficient hydrogen production from partial oxidation of propane over SiC doped Ni/Al₂O₃ catalyst. *Energy Procedia* **2019**, *158*, 1772–1779. [[CrossRef](#)]
97. Spanou, S.; Kontos, A.I.; Siokou, A.; Kontos, A.G.; Vaenas, N.; Falaras, P.; Pavlatou, E.A. Self cleaning behaviour of Ni/nano-TiO₂ metal matrix composites. *Electrochim. Acta* **2013**, *105*, 324–332. [[CrossRef](#)]
98. Billo, T.; Fu, F.-Y.; Raghunath, P.; Shown, I.; Chen, W.-F.; Lien, H.-T.; Shen, T.-H.; Lee, J.-F.; Chan, T.-S.; Huang, K.-Y.; et al. Ni-Nanocluster Modified Black TiO₂ with Dual Active Sites for Selective Photocatalytic CO₂ Reduction. *Small* **2018**, *14*, 1702928. [[CrossRef](#)]

99. Zhou, J.; Zhang, Y.; Li, S.; Chen, J. Ni/NiO Nanocomposites with Rich Oxygen Vacancies as High-Performance Catalysts for Nitrophenol Hydrogenation. *Catalysts* **2019**, *9*, 944. [[CrossRef](#)]
100. Garbarino, G.; Riani, P.; Infantes-Molina, A.; Rodríguez-Castellón, E.; Busca, G. On the detectability limits of nickel species on NiO/ γ -Al₂O₃ catalytic materials. *Appl. Catal. A Gen.* **2016**, *525*, 180–189. [[CrossRef](#)]
101. Panagiotou, G.D.; Petsi, T.; Bourikas, K.; Kordulis, C.; Lycourghiotis, A. The interfacial chemistry of the impregnation step involved in the preparation of tungsten(VI) supported titania catalysts. *J. Catal.* **2009**, *262*, 266–279. [[CrossRef](#)]
102. Cruz-Perez, A.E.; Guevara-Lara, A.; Morales-Ceron, J.P.; Alvarez-Hernandez, A.; Reyes, J.A.D.L.; Massin, L.; Geantet, C.; Vrinat, M. Ni and W interactions in the oxide and sulfide states on an Al₂O₃-TiO₂ support and their effects on dibenzothiophene hydrodesulfurization. *Catal. Today* **2011**, *172*, 203–208. [[CrossRef](#)]
103. Parry, E.P. An infrared study of pyridine adsorbed on acidic solids. Characterization of surface acidity. *J. Catal.* **1963**, *2*, 371–379. [[CrossRef](#)]
104. Zaki, M.I.; Hasan, M.A.; Al-Sagheer, F.A.; Pasupulety, L. In situ FTIR spectra of pyridine adsorbed on SiO₂-Al₂O₃, TiO₂, ZrO₂ and CeO₂: General considerations for the identification of acid sites on surfaces of finely divided metal oxides. *Colloids Surf. A Physicochem. Eng. Asp.* **2001**, *190*, 261–274. [[CrossRef](#)]
105. Mohan, V.; Raghavendra, C.; Pramod, C.V.; Raju, B.D.; Rama Rao, K.S. Ni/H-ZSM-5 as a promising catalyst for vapour phase hydrogenation of levulinic acid at atmospheric pressure. *RSC Adv.* **2014**, *4*, 9660–9668. [[CrossRef](#)]
106. Leal, G.F.; Lima, S.; Graça, I.; Carrer, H.; Barrett, D.H.; Teixeira-Neto, E.; Curvelo, A.A.S.; Rodella, C.B.; Rinaldi, R. Design of Nickel Supported on Water-Tolerant Nb₂O₅ Catalysts for the Hydrotreating of Lignin Streams Obtained from Lignin-First Biorefining. *iScience* **2019**, *15*, 467–488. [[CrossRef](#)] [[PubMed](#)]
107. Tanabe, K. (Ed.) Chapter 2—Determination of Acidic Properties on Solid Surfaces. In *Solid Acids and Bases*; Academic Press: London, UK, 1970; pp. 5–33.
108. Tanabe, K. (Ed.) Chapter 4—Acid and Base Centres: Their Structure and Acid-Base Properties. In *Solid Acids and Bases*; Academic Press: London, UK, 1970; pp. 45–101.
109. Busca, G.; Lorenzelli, V.; Escribano, V.S.; Guidetti, R. FT-113 study of the surface properties of the spinels NiAl₂O₄ and CoAl₂O₄ in relation to those of transitional aluminas. *J. Catal.* **1991**, *131*, 167–177. [[CrossRef](#)]
110. Venezia, A.M.; Bertocello, R.; Deganello, G. X-ray photoelectron spectroscopy investigation of pumice-supported nickel catalysts. *Surf. Interface Anal.* **1995**, *23*, 239–247. [[CrossRef](#)]
111. Li, C.P.; Proctor, A.; Hercules, D.M. Curve Fitting Analysis of ESCA Ni 2p Spectra of Nickel-Oxygen Compounds and Ni/Al₂O₃ Catalysts. *Appl. Spectrosc.* **1984**, *38*, 880–886. [[CrossRef](#)]
112. Ruan, L.; Zhang, H.; Zhou, M.; Zhu, L.; Pei, A.; Wang, J.; Yang, K.; Zhang, C.; Xiao, S.; Chen, B.H. A highly selective and efficient Pd/Ni/Ni(OH)₂/C catalyst for furfural hydrogenation at low temperatures. *Mol. Catal.* **2020**, *480*, 110639. [[CrossRef](#)]
113. Zhang, L.; Wang, X.; Chen, C.; Zou, X.; Shang, X.; Ding, W.; Lu, X. Investigation of mesoporous NiAl₂O₄/MO_x (M = La, Ce, Ca, Mg)- γ -Al₂O₃ nanocomposites for dry reforming of methane. *RSC Adv.* **2017**, *7*, 33143–33154. [[CrossRef](#)]
114. Liu, Y.; Liu, F.; Bai, J.; Liu, T.; Yu, Z.; Dai, M.; Zhou, L.; Wang, H.; Zhang, Y.; Suo, H.; et al. Direct growth of NiO films on Al₂O₃ ceramics by electrochemical deposition and its excellent H₂S sensing properties. *Sens. Actuators B Chem.* **2019**, *296*, 126619. [[CrossRef](#)]
115. Méndez-Mateos, D.; Barrio, V.L.; Requies, J.M.; Cambra, J.F. A study of deactivation by H₂S and regeneration of a Ni catalyst supported on Al₂O₃, during methanation of CO₂. Effect of the promoters Co, Cr, Fe and Mo. *RSC Advances* **2020**, *10*, 16551–16564. [[CrossRef](#)]
116. Rodríguez, J.L.; Poznyak, T.; Valenzuela, M.A.; Tiznado, H.; Chairez, I. Surface interactions and mechanistic studies of 2,4-dichlorophenoxyacetic acid degradation by catalytic ozonation in presence of Ni/TiO₂. *Chem. Eng. J.* **2013**, *222*, 426–434. [[CrossRef](#)]
117. Reddy, B.M.; Chowdhury, B.; Reddy, E.P.; Fernández, A. An XPS study of dispersion and chemical state of MoO₃ on Al₂O₃-TiO₂ binary oxide support. *Appl. Catal. A Gen.* **2001**, *213*, 279–288. [[CrossRef](#)]
118. Zhao, X.; Xie, W.; Deng, Z.; Wang, G.; Cao, A.; Chen, H.; Yang, B.; Wang, Z.; Su, X.; Yang, C. Salt templated synthesis of NiO/TiO₂ supported carbon nanosheets for photocatalytic hydrogen production. *Colloids Surf. A Physicochem. Eng. Asp.* **2020**, *587*, 124365. [[CrossRef](#)]
119. Riyapan, S.; Boonyongmaneerat, Y.; Mekasuwandumrong, O.; Praserthdam, P.; Panpranot, J. Effect of surface Ti³⁺ on the sol-gel derived TiO₂ in the selective acetylene hydrogenation on Pd/TiO₂ catalysts. *Catal. Today* **2015**, *245*, 134–138. [[CrossRef](#)]
120. Xu, J.; Sun, K.; Zhang, L.; Ren, Y.; Xu, X. A highly efficient and selective catalyst for liquid phase hydrogenation of maleic anhydride to butyric acid. *Catal. Commun.* **2005**, *6*, 462–465. [[CrossRef](#)]
121. Patra, N.; Karuturi, S.K.; Vasa, N.J.; Nakamura, D.; Higashihata, M.; Singh, V.; Palani, I. Influence of Ni, Ti and NiTi alloy nanoparticles on hydrothermally grown ZnO nanowires for photoluminescence enhancement. *J. Alloys Compd.* **2019**, *770*, 1119–1129. [[CrossRef](#)]
122. Capel-Sanchez, M.C.; Campos-Martin, J.M.; Fierro, J.L.G.; de Frutos, M.P.; Polo, A.P. Effective alkene epoxidation with dilute hydrogen peroxide on amorphous silica-supported titanium catalysts. *Chem. Commun.* **2000**, 855–856. [[CrossRef](#)]
123. Reddy, B.M.; Chowdhury, B.; Smirniotis, P.G. An XPS study of the dispersion of MoO₃ on TiO₂-ZrO₂, TiO₂-SiO₂, TiO₂-Al₂O₃, SiO₂-ZrO₂, and SiO₂-TiO₂-ZrO₂ mixed oxides. *Appl. Catal. A Gen.* **2001**, *211*, 19–30. [[CrossRef](#)]

124. Reddy, Y.A.K.; Ajitha, B.; Sreedhar, A.; Varrla, E. Enhanced UV photodetector performance in bi-layer TiO₂/WO₃ sputtered films. *Appl. Surf. Sci.* **2019**, *494*, 575–582. [[CrossRef](#)]
125. Chen, C.; Xu, M.; Zhang, K.; An, H.; Zhang, G.; Hong, B.; Li, J.; Lai, Y. Atomically ordered and epitaxially grown surface structure in core-shell NCA/NiAl₂O₄ enabling high voltage cyclic stability for cathode application. *Electrochim. Acta* **2019**, *300*, 437–444. [[CrossRef](#)]
126. Yan, L.; Yao, Q.; Fu, Y. Conversion of levulinic acid and alkyl levulinates into biofuels and high-value chemicals. *Green Chem.* **2017**, *19*, 5527–5547. [[CrossRef](#)]
127. Pham, T.N.; Shi, D.; Resasco, D.E. Reaction kinetics and mechanism of ketonization of aliphatic carboxylic acids with different carbon chain lengths over Ru/TiO₂ catalyst. *J. Catal.* **2014**, *314*, 149–158. [[CrossRef](#)]
128. Tukacs, J.M.; Sylvester, Á.; Kmecz, I.; Jones, R.V.; Óvári, M.; Mika, L.T. Continuous flow hydrogenation of methyl and ethyl levulinate: An alternative route to γ -valerolactone production. *R. Soc. Open Sci.* **2019**, *6*, 182233. [[CrossRef](#)] [[PubMed](#)]
129. Abdelrahman, O.A.; Heyden, A.; Bond, J.Q. Analysis of Kinetics and Reaction Pathways in the Aqueous-Phase Hydrogenation of Levulinic Acid To Form γ -Valerolactone over Ru/C. *ACS Catal.* **2014**, *4*, 1171–1181. [[CrossRef](#)]
130. Weng, R.; Yu, Z.; Xiong, J.; Lu, X. Effects of water in the heterogeneous catalytic valorization of levulinic acid into γ -valerolactone and its derivatives. *Green Chem.* **2020**, *22*, 3013–3027. [[CrossRef](#)]
131. Sosa, L.F.; da Silva, V.T.; de Souza, P.M. Hydrogenation of levulinic acid to γ -valerolactone using carbon nanotubes supported nickel catalysts. *Catal. Today* **2020**, *381*, 86–95. [[CrossRef](#)]
132. Song, S.; Yao, S.; Cao, J.; Di, L.; Wu, G.; Guan, N.; Li, L. Heterostructured Ni/NiO composite as a robust catalyst for the hydrogenation of levulinic acid to γ -valerolactone. *Appl. Catal. B Environ.* **2017**, *217*, 115–124. [[CrossRef](#)]
133. Im, J.; Shin, H.; Jang, H.; Kim, H.; Choi, M. Maximizing the catalytic function of hydrogen spillover in platinum-encapsulated aluminosilicates with controlled nanostructures. *Nat. Commun.* **2014**, *5*, 3370. [[CrossRef](#)]
134. Cheng, Z.X.; Zhao, X.G.; Li, J.L.; Zhu, Q.M. Role of support in CO₂ reforming of CH₄ over a Ni/ γ -Al₂O₃ catalyst. *Appl. Catal. A Gen.* **2001**, *205*, 31–36. [[CrossRef](#)]
135. Mieth, J.A.; Huang, Y.J.; Schwarz, J.A. Experimental procedures to evaluate dissolution, metal ion buffering, and catalytic precursor speciation during catalyst preparation. *J. Colloid Interface Sci.* **1988**, *123*, 366–379. [[CrossRef](#)]
136. Huang, Y.J.; Schwarz, J.A.; Diehl, J.R.; Baltrus, J.P. Effect of Catalyst Preparation on Catalytic Activity: V. Chemical Structures on Nickel/Alumina Catalysts. *Appl. Catal.* **1988**, *36*, 163–175. [[CrossRef](#)]